MULTIFERROIC PROPERTIES OF MAGNETIC-ION-SUBSTITUTED OXIDE-ELECTROCERAMIC THIN FILMS

by

Danilo Gregorio Barrionuevo-Diestra

A thesis submitted in partial fulfillment of the requirements for the degree of

MASTER OF SCIENCE
in
PHYSICS

UNIVERSITY OF PUERTO RICO
MAYAGÜEZ CAMPUS
2010

Approved by:

_____   _____
Surinder P. Singh, Ph.D.   Date
Member of the Graduate Committee

_____   _____
Hector Jiménez-González, Ph.D.   Date
Member of the Graduate Committee

_____   _____
Maharaj S. Tomar, Ph.D.   Date
President of the Graduate Committee

_____   _____
Elsie I. Parés-Matos, Ph.D.   Date
Representative of Graduate Studies

_____   _____
Hector Jiménez-González, Ph.D.   Date
Chairperson of the Department

ABSTRACT

Materials which possess electrical and magnetic coupling are of great interest for novel devices. In this thesis, $BiFe_{1-x}D_xO_3$ (D= Co, Cr and Mn) material system were synthesized by solution route for various compositions, and thin films were prepared by spin coating on Pt ($Pt/Ti/SiO_2/Si$) substrates. Structural properties of the films were investigated by X-ray diffraction and Raman spectroscopy. X-ray diffraction patterns confirms an intense (110) peak in BiFeO3 and $BiFe_{1-x}D_xO_3$ (D= Co, Cr and Mn) composites. Observed diffraction peaks for $BiFe_{1-x}D_xO_3$ (D= Co, Cr and Mn) suggests the formation of rhombohedral perovskite structure with the space group R3c. $BiFe_{1-x}D_xO_3$ (D= Co, Cr and Mn) films show a weak ferroelectric polarization and ferromagnetism at room temperature. Ferroelectric and ferromagnetic behavior in the same phase could be attributed to the elimination of oxygen vacancies and increased stress in the crystal structure. In addition, some results are shown of new composite materials, which show both ferroelectric and ferromagnetic behavior.

RESUMEN

Los materiales que poseen un acoplamiento eléctrico y magnético son de gran interés para los nuevos dispositivos. En esta tesis, el sistema de materiales $BiFe_{1-x}D_xO_3$ (D= Co, Cr and Mn), fue sintetizado por la ruta de solución a varias composiciones, y las películas delgadas fueron preparadas por medio del metodo "spin-coating" sobre sustratos de platino ($Pt/Ti/SiO_2/Si$). Las propiedades estructurales de las películas fueron investigadas por los estudios de difracción de rayos X y por espectroscopia Raman. Los patrones de difracción de rayos X confirman la presencia de un intenso pico (110) de $BiFe_{1-x}D_xO_3$ (D= Co, Cr and Mn). Se observaron picos de difracción en $BiFe_{1-x}D_xO_3$ (D= Co, Cr and Mn) los cuales sugieren la formación de la estructura perovskita con romboédricos en el espacio de grupo R3c. Las películas de $BiFe_{1-x}D_xO_3$ (D= Co, Cr and Mn) muestran una débil polarización ferroeléctrica y ferromagnetismo a temperatura ambiente. El comportamiento ferroeléctrico y ferromagnético en la misma fase puede atribuirse a la eliminación de vacantes de oxígeno y a la tensión creciente en la estructura cristalina. Además, algunos resultados de nuevos materiales compuestos son mostrados, cuales muestras ambos comportamientos ferroeléctrico y ferromagnético.

DEDICATORY

To God, for his infinite love.

This thesis is dedicated to my parents Gregorio Barrionuevo and Fermina Diestra, and my brothers Hugo, Olinda and Percy. They teached me that the best kind of knowledge to have is that which is learned for its own sake and that even the largest task can be accomplished if it is done one step at a time.

ACKNOWLEDGMENT

First, I would like to say thank you to our creator, God. Thank you my Lord to help me with my goals, especially my master degree. Believing in you makes me to understand, with conviction, to go through any obstacle in this life. Thank you, for your help and for making me with patience, constancy and a successful person. In this stage of my life when I am concluding one of my dreams, I have to include as part of this achievement, every person that helped me to be here.

Thanks to my parents, Gregorio Barrionuevo-Padilla and Fermina Diestra-Azaña, and to my brothers Olinda, Hugo and Percy Barrionuevo-Diestra. Thank you for always be there and be my inspiration. Having all of you as my family makes me feel grateful and enviable to know that in any place and any situation, I can count on all of you. To Hilda L. Haro-De la Cruz, thank you for your unconditional help. Thank you to be part of my life and give me the opportunity to know, a beautiful person.

Thanks to my advisor, Dr. Maharaj S. Tomar, for guiding me throughout the course of this work.

Thanks to Dr. Surinder P. Singh, for his help in the laboratory, his advice and unconditional disposition.

Thanks to Dr. Ram S. Katiyar, Dr. Ricardo Melgarejo, Ricardo Martínez, for providing me the use of the measurement facility at UPR-Rio Piedras Campus.

Thanks to Dr. Oscar Perales and Ms. Boris Renteria (Department of Engineering Science and Materials) for their valuable help with the Ferromagnetic (VSM), and Dr. Samuel Hernández and Ms. Leonardo Pacheco (Chemistry Department) for their valuable help with the Raman instrumentation.

Thanks to the University of Puerto Rico at Mayagüez, for this amazing opportunity for letting know wonderful researchers, and better person. Thanks to the teaching appointment in Physics and in Life.

Thanks to DoE-EPSCoR Grant No. DE-SG02-08ER46526 that support me for all this period of my research work.

TABLE OF CONTENTS

LIST OF TABLES

LIST OF FIGURES

xiv

1. INTRODUCTION

Multiferroics are a class of materials which exhibit two or more of the ferroic orders, namely ferroelectric, ferromagnetic and ferroelastic [51]. This classification of multiferroics has been extended to include antiferroic ordering also. However, it has become a trend to use the term "multiferroics" to mean the materials which have both spontaneous magnetic and electrical ordering simultaneously [52]. If there is a coupling between their order parameters, these materials exhibit an interesting physical phenomenon called the magnetoelectric (ME) effect. It opens up a number of new applications, such as switching of magnetic memory elements by electric fields.

$BiFeO_3$ (BFO) has attracted a lot of attention as a magnetoelectric multiferroic material, which has been expected to show a magnetoelectric coupling effect at room temperature, since both ferroelectric and antiferromagnetic transition temperatures are much higher than room temperature [52]. However, the high leakage current of BFO limits its dielectric property. A small amount of donor ions were substituted for Fe^{3+} ions in BFO in order to investigate the ferroelectric and the magnetic properties of BFO.

Therefore, magnetic ions, such as cobalt (Co), chromium (Cr) and manganese (Mn), were doped into BFO bulk to improve the magnetic properties. Even though the Mn-doping did not improve the magnetic properties of BFO, the (Co and Cr)-doped BFO showed the significantly enhanced magnetization [85, 86].

Based on the results of the sintered body of doped BFO, the experiments of the BFO thin film deposition by Chemical Solution Deposition (CSD) method were performed. In case of CSD method, the leakage current of undoped BFO thin film could be reduced by controlling the crystallographic orientation, and could be adjusted by changing the pyrolysis temperature. When the polycrystalline BFO film was deposited by CSD method, the incorporation of donor dopants into BFO thin film decreased the leakage current in the similar way to the BFO bulk.

In search of new multiferroics, the alternate multilayers of ferroelectric and ferromagnetic materials were also investigated, which showed both ferroelectric and magnetic properties at room temperature. It is suggested that a possible electric and magnetic coupling parameters are present in multilayer composite structure [52]. The results of structural, ferroelectric and ferromagnetic properties are present in this work.

For any practical device, the magnetic and electric coupling is desired at room temperature.

2. THEORETICAL BACKGROUND

2.1 Crystal Structure

BiFeO$_3$ (BFO) is one of the single phase multiferroic materials with high ferroelectric Curie (T_C =830 °C) and antiferromagnetic Néel (T_N =370 °C) temperatures that makes it attractive for magnetoelectric applications [1]. For this reason, there have been extensive studies of the structure and properties of bulk and thin film BFO. Bulk BFO has a rhombohedrally distorted perovskite structure (a_{rh}=5.6343 Å and α_{rh}=59.348°) with space group $R3c$ [2, 3]. Figure 2.1 shows the structure of a primitive unit cell of BFO, which contains two formula units (ten atoms), arising from counter rotations of neighboring O octahedra about the [111] axis [3]. The displacement of Bi, Fe, and O ions from their ideal positions along the [111] axis results in spontaneous polarization along [111]. BFO exhibits a G-type antiferromagnetic ordering, where the Fe magnetic moments are aligned ferromagnetically within the (111) planes and antiferromagnetically between the adjacent (111) planes [4]. Bulk BFO exhibits also a spiral spin structure, where the antiferromagnetic axis rotates through the crystal with a long wavelength period, superimposed on the antiferromagnetic ordering of 620 Å, which cancels macroscopic magnetization leading to an extremely small saturation magnetization [5].
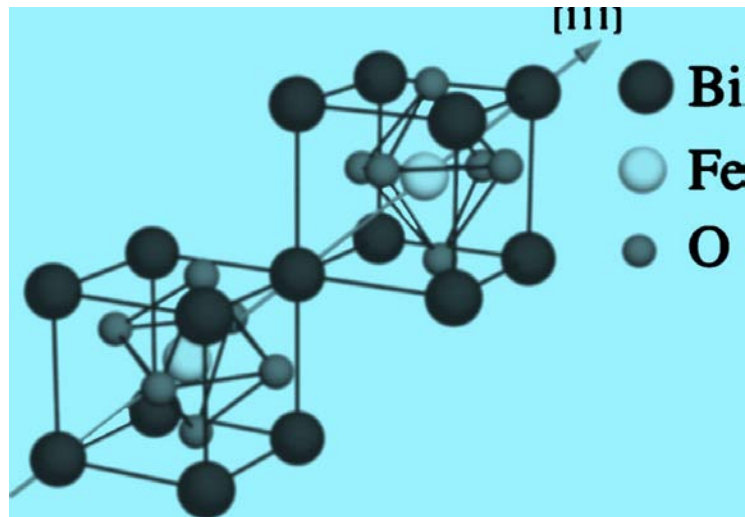
Figure 2.1 Structure of R3c BiFeO$_3$. Notice the position of the oxygen octahedral relative to the Bi framework; in the ideal cubic perovskite structure the oxygen ions would occupy the face centered sites [3].

Today, there are several challenges facing BFO that must be overcome before this material can be considered suitable for practical applications. These challenges are *i*) high leakage current, *ii*) small remnant polarization, *iii*) high coercive field, and *iv*) inhomogeneous magnetic spin structure [6]. Of these challenges, large leakage current is the most serious factor limiting the applications of BFO. The large leakage current is usually attributed to deviation from oxygen stoichiometry, which leads to the change in oxidation state of Fe ions (from Fe^{3+} to Fe^{2+}) in order to compensate for the charge of oxygen vacancies. The coexistence of Fe^{3+} and Fe^{2+} causes electron hopping between Fe^{3+} and Fe^{2+} ions, oxygen vacancies acting as a bridge between them, which increases the leakage current [7-9].

The inhomogeneous spin structure results from the spatially modulated, cycloidal spin structure with the periodicity of about 620 Å, which is incommensurate with the crystallographic lattice parameters [10]. Several approaches have been proposed to overcome the spiral spin structure, among which are doping and formation of $BiFeO_3$ based solid solutions [11-13] and application of high magnetic field [11, 14] and strain [15, 16]. Until recently, the value of polarization in bulk BFO was considered to be small, with spontaneous polarization on the order of a few $\mu C/cm^2$ and non-saturated hysteresis loops [17].

However; epitaxial BFO films have attracted significant interest when strong multiferroic behavior together with large values of magnetization and electric polarization were reported by Wang et al. in 2003 [15]. For BFO films epitaxially grown on $SrTiO_3$ substrates, they found very high spontaneous polarization up to 50-60 $\mu C/cm^2$, one order of magnitude higher than that for bulk BFO, and a saturation magnetization of 150 emu/cm^3. The magnetization was stated to be dependent on the film thickness. The huge difference in the properties of the BFO films from the bulk material was attributed to the difference in the crystal structure of the thin films under investigation caused by the mismatch strain. It should be noted however that, although large polarization values for BFO films were also reported by other groups [18-23], Wang et al. [15] reported such high values of magnetization, and the accuracy of the data as well as the mechanism of the enhancement of magnetization and polarization is still under discussion [24, 25]. BFO layers were grown by all the conventional growth methods such as PLD, [15-20] MOCVD, [26, 27] chemical solution deposition (CSD), [28, 29] RF sputtering, [30, 31] and sol-gel [32, 33]. Epitaxial BFO films show much higher polarization values that bulk samples [18-21, 23] which is consistent with theoretical considerations [3, 22] and can be

explained by improved crystal quality and stoichiometry, different structural modifications stabilized in the thin films, [20, 23] or within the modern theory of polarization [3, 34-36].

Structural and physical properties of epitaxially grown BFO films were found to depend on ambient oxygen pressure during PLD growth [18, 20, 37]. For example, Yun et al. have found that the crystal structure and lattice constant of BFO films depend strongly on the oxygen pressure [20]. In this study, the BFO films deposited at various oxygen pressures were single phase with a tetragonally destorted perovskite structure, in spite of the fact that bulk BFO is known to be a rhombohedrally distorted perovskite [20]. The c/a ratio of the films decreased from 1.032 to 1.014 as the oxygen pressure decreased from 0.15 to 0.005 Torr. The tetragonal distortion in epitaxmoial BFO films is attributed generally to the mismatch strain, and the dependence of the c/a ratio on the oxygen pressure was attributed by the authors to both the lattice strain and oxygen stoichiometry in the films [20].

Fujino et al. deposited BFO thin films by ablating a $Bi_{1.1}FeO_3$ target with a KrF excimer laser ($\lambda = 248$ nm) at a typical fluence of 2 J/cm^2 [37]. The oxygen pressure during deposition was varied in the range from 10^{-4} to 10^{-1} Torr, and the substrate temperature was kept constant at 600°C. Epitaxial BFO films with (001) orientation were obtained at oxygen pressures above 1 $\times 10^{-3}$ Torr. Figure 2.2 shows the phase composition of the BFO films as a function of oxygen pressure. At low pressures ($< 2 \times 10^{-2}$ Torr), the Fe_2O_3 phase was found in the BFO films, and the portion of the Fe_2O_3 increased as the oxygen pressure decreased. Pure BFO phase was identified by x-ray diffraction for a pressures range from 5×10^{-3} Torr to 5×10^{-2} Torr. At high oxygen pressures ($> 5 \times 10^{-2}$ Torr), the Bi_2O_3 phase was observed, and the Bi_2O_3 content in the films increased with pressure.
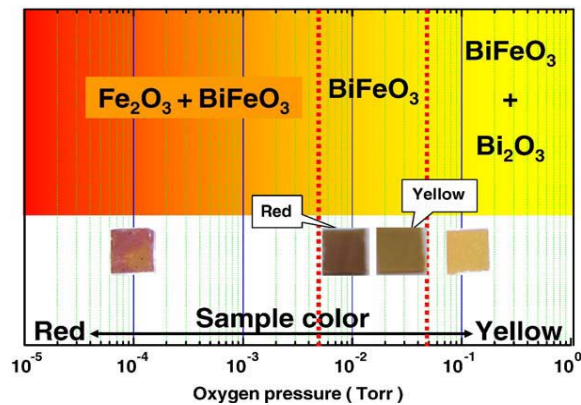
Figure 2.2   Summary of phases present in BFO films as a function of oxygen deposition pressure as determined by XRD analysis. The sample color changes from yellow to red [37].

2.2 Ferromagnetic effect

Ferromagnetic materials are magnetic materials; the mechanisms responsible for magnetization and the related ferromagnetic behavior are complicated and must be treated quantum mechanically, which is beyond the scope of the present work. However, for completeness we shall discuss briefly, and only qualitatively, the origins of ferromagnetic behavior. General ferromagnetic properties are summarized as follows:

• The magnetization is spontaneous.

• The magnetization may reach a saturation value by a weak magnetizing field.

• The material may have zero magnetization at zero (or very small) magnetic fields, and the magnetization remains after the removal of the magnetic field. Thus, when the applied magnetic field is changed from a positive polarity to a negative polarity and then back to the positive polarity, a hysteresis loop will be formed in the relation of B and H, resulting in energy loss due to the rotation of the dipoles. The area enclosed by the hysteresis loop represents the energy loss involved.

• The ferromagnetic behavior (i.e., the spontaneous magnetization) completely disappears at temperatures higher than a critical temperature, called the Curie temperature T_C. At $T > T_C$, spontaneous magnetization is destroyed, and the material becomes paramagnetic, not ferromagnetic [38].

The commonly used ferromagnetic materials are iron (Fe), cobalt (Co), nickel (Ni), and their alloys, which are of importance to technical applications. The Curie temperatures for Fe, Co and Ni are respectively 1043 K, 1400 K and 630 K [38]. However, the elemental metals and their alloys are metallic in nature, and their electric conductivity is generally very high. For some applications, insulating or semi-insulating ferromagnetic materials are preferable. Some oxides, such as CrO_2, $MnOFe_2O_3$, and $FeOFe_2O_3$, have low electric conductivity and also possess spontaneous magnetization under suitable circumstances [39]. They have a reasonable range of Curie temperatures much higher than normal room temperature. In all of the elemental metals, spontaneous magnetization arises from an incomplete 3d shell for Fe, Co, and Ni. In this section, we use Fe as an example to discuss the mechanisms of ferromagnetic behavior. The same mechanisms apply to other elements with incomplete 3d.

An iron atom has six electrons in the 3d shell; a fully filled 3d shell should contain ten electrons. Of these six electrons in the 3d shell, five spin in the same direction and only one spins in the opposite direction. This makes the spin magnetic dipole moment of one atom equal to $4u_B$ [39]. Why are these six electrons in the 3d shell divided in such a way that five electrons have the same spin and only one electron has the opposite spin, producing a net spin magnetic moment of $4u_B$? In other words, why must these six electrons form a magnetized state (with five electrons in one spin and one in opposite spin), instead of having a nonmagnetized state (three electrons in one spin and the other three in opposite spin)? This can only be explained through quantum mechanics [39].

The exchange energy principle, coupled with the Pauli's Exclusion Principle, shows that the potential energy of the electrons in the magnetized state is lower than when they are in the nonmagnetized state [40]. This conclusion can also be realized on the basis of band theory, by considering that the electrons with up-spin form one band and those with down-spin form another. These two bands would be completely filled if there were ten electrons in the 3d shell per atom, i.e., five electrons with up-spin and the other five with down-spin. However, iron atoms have only six electrons in the 3d shell. For the unmagnetized state, we would expect three electrons in the up-spin band and the other three in the down-spin band. In this case, both bands are partially filled. For the magnetized state, we would expect five electrons with same spin in one band, which is completely filled, and one electron with opposite spin in the other band, which is partially filled. By comparing these two states, it can be imagined that the magnetized state is more stable than the unmagnetized one. This also implies that the potential energy is lower in the magnetized state than in the unmagnetized state, because for the former, one band is completely filled, while for the latter, each band is only partially filled [41]. However, the difference in potential energy between these two states, referred to as the exchange energy, is small; it is of the order of 0.1eV [41].

Thermal agitation tends to destroy such a magnetized state (the state with a minimum potential energy) and hence, the spontaneous magnetization. Thus, we would expect that there is a critical temperature, at or above which the magnetized state would become an unmagnetized state, and spontaneous magnetization would be completely destroyed. This critical temperature is called the Curie temperature T_C [41]. Its value is different for different magnetic materials, as mentioned previously. Ferromagnetic materials, such as Fe, Co, and Ni, have definite types of

crystalline structure, such as body-centered cubic for Fe, hexagonal for Co, and face-centered cubic for Ni [41]. In such crystals, there are certain principal directions, which are (100), (110), and (111), assigned according to the Miller system of indices.

In general, for body-centered cubic Fe, magnetization is easy in the (100) direction, medium in (110), and hard in (111) [41]. Most magnetic materials are polycrystalline, i.e., the material is composed of a large number of very tiny single crystals, called grains. Between grains, there exist grain boundaries. In each grain, there are many spin magnetic dipoles. Even their magnetic moments tend to be parallel to the easy direction, but there are six possible easy directions in a cubic unit cell: $\pm$ x, $\pm$ y and $\pm$ z. In order to reduce the dipole interaction energy (i.e., magnetostatic or magnetic field energy) to a minimal or lowest level, the grain must be divided into many small regions called domains [41]. In each domain, the net spin magnetic moments are pointing in one easy direction, which is termed the parallel direction or in the reverse easy direction, which is termed the antiparallel direction [41]. At $T = 0$, all spins in one domain will be pointing in the parallel direction and this domain is said to be spontaneously magnetized to the maximum degree without the aid of any external magnetic fields.

The formation of domains inside a crystal is a natural process to minimize the potential energy of the system, which contains a large number of spin magnetic dipole moments. It can be imagined that, if the crystal had only one domain with a net magnetic moment pointing in one direction, this magnetic moment would be large and produce a large external magnetic field; therefore, a large amount of energy is involved, as shown in Figure 2.3(a). However, if the crystal is divided into four or more domains with the magnetic moments in the domains tending to cancel one another out, as shown in Figure 2.3(b), then a lower energy for the crystal can be achieved. The mutual reaction force between the dipoles pointing in one direction acts as a driving force to cause the formation of more domains, with the magnetic moments pointing different directions so that they can cancel one another, thus reducing the potential energy of the system. The partial distribution of domains tends to assume the configuration so that adjacent domains have opposite magnetic moments. Some possible configurations are shown in Figure 2.3(c). The potential magnetic energy in Figure 2.3(c) part I is smaller than that in Figure 2.3(a), and the potential energy in Figure 2.3(c) parts III and IV is much smaller than that in Figure 2.3(c) part II. It seems that the larger the number of domains formed, the lower the energy associated with the system.

But when domains are formed, block walls (or domain walls) are required to separate the domains.

Energy is required to create a wall between domains. This, in turn, results in an increase of the energy in the system. It is likely that the increase in energy for the creation of domain walls balances the decrease in energy due to the formation of domains. There must be an

a)

b)

c)
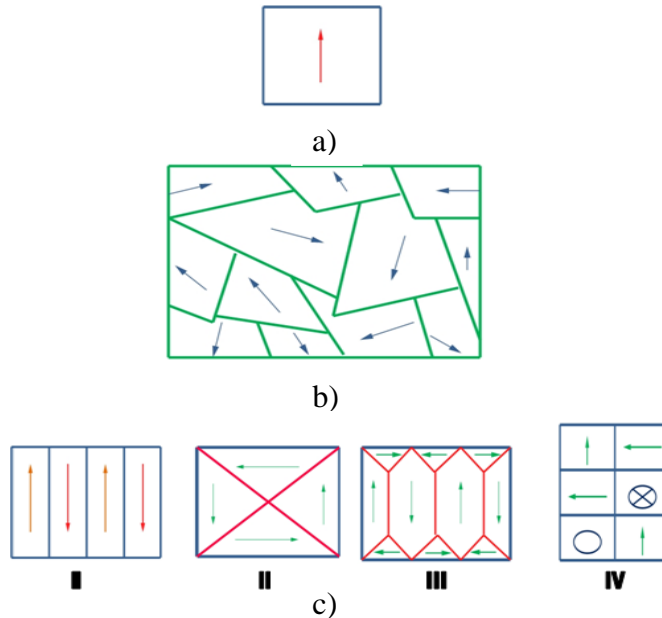
Figure 2.3   Schematic diagrams showing the directions of spin magnetic moments in the domains inside a piece of ferromagnetic material. (a) net magnetic moment pointing in only one direction with a large potential energy; (b) each domain having its magnetic moment pointing in different directions with a total minimal potential energy; (c) some possible configurations, the magnetic moment pointing into the plane of the page and the magnetic moment pointing out of it. The potential energy is lower with the magnetic moments of neighboring domains pointing in opposite directions [41].

optimal point at which the number of domains is limited by the minimization of the total energy of the system. In other words, the number and the configuration of domains in a magnetic material are determined by the minimization of the magnetic field energy and the domain wall energy. The domain wall energy arises from both the exchange energy and the isotropy energy; the former is related to the energy difference between the unmagnetized state and the magnetized state, while the latter is related to the energy involved for magnetization in one direction relative to the crystal axes and in another direction [41]. In a material as a whole, there are many tiny

crystals (grains), and each grain has many domains. The magnetic moments are pointing randomly in all directions, resulting in a zero net magnetization, as shown in Figure 2.3(c). It is desirable to have a general picture about the sizes of grains and domains. Suppose a piece of iron of one cubic centimeter (cm^3) has about 10^{23} atoms, which may contain about 10^4 tiny single crystals (grains), and each grain may be divided into about 10^5 domains in average.

This means that in average, there are about 10^{19} atoms per grain and about 10^{14} atoms per domain. Assuming that both the grain and the domain are cubic in shape, the linear dimensions would be about 5×10^{-2} cm for a grain and about 10^{-3} cm for a domain. Note that the sizes of the grains and the domains may be different from grain to grain and from domain to domain, and their shape is not necessarily cubic. The example given here is only to establish a feeling about the average sizes of a grain and a domain. Let us now consider the influence of an applied magnetic field on the orientation of the magnetic moments in the domains toward the direction of the magnetic field H to produce an overall magnetization of the whole material. Suppose that we apply a magnetic field H to a nonmagnetized ferromagnetic solid, starting with zero fields and gradually increasing the field in steps. We can see the gradual increase of the magnetization M, as shown in Figure 2.4(a). The M-H curve has four regions; each is related to different magnetization processes:

• Region I: Magnetization by translation increasing the size of the magnetized domains parallel to H and reducing the size of those with magnetization antiparallel to H, as shown in Figure 2.4(b).
• Region II: M increases in a series of jerky steps with increasing H, corresponding to jerky rotation of domains from the original "easy" crystal direction to other "easy" direction more nearly parallel to H. This phenomenon is known as the Barkhausen effect.
• Region III: The magnetic moments in all domains rotate gradually from the "easy" direction toward the direction of H.
• Region IV: Further increase in H will make the magnetic moments of all domains parallel to H, implying that the magnetization has reached a saturation value.

Now we start to reduce the magnetic field H, also in steps. As can be seen in Figure 2.4(a), M at point 5 is almost the same as at point 4, but with further decrease of H to

zero, M does not go back to zero, but decreases following a different curve and reaches a finite value M_R at H = 0. M_R is referred to as the remnant magnetization. To bring M to zero, we need a reverse magnetic field -H_C, which is generally called the coercive force or demagnetizing field. This is the magnetic field opposite to the magnetization field, required to bring the magnetization to the vanishing point. The formation of a hysteresis loop implies that the magnetization of a ferromagnetic material is irreversible. The paths 3-4 and 4-5 are almost identical, indicating that the domains' rotation from an "easy" to a "hard" direction is reversible. However, the paths 0-1-2-3 and 5-6-7 are quite different, indicating that the domain motion is irreversible because of the unavoidable presence of all kinds of defects: structural defects and chemical defects or impurities in a real material.

The domain walls move in a series of jerky steps or in a jerky rotation due to the collision with various defects, which consume energy [41]. When a magnetization process consumes energy, this process will be irreversible, and this is why a hysteresis loop is formed [41]. For the hysteresis loop around the loop 5-6-7-8-11-12-5, the hysteresis loss is equal to the loop
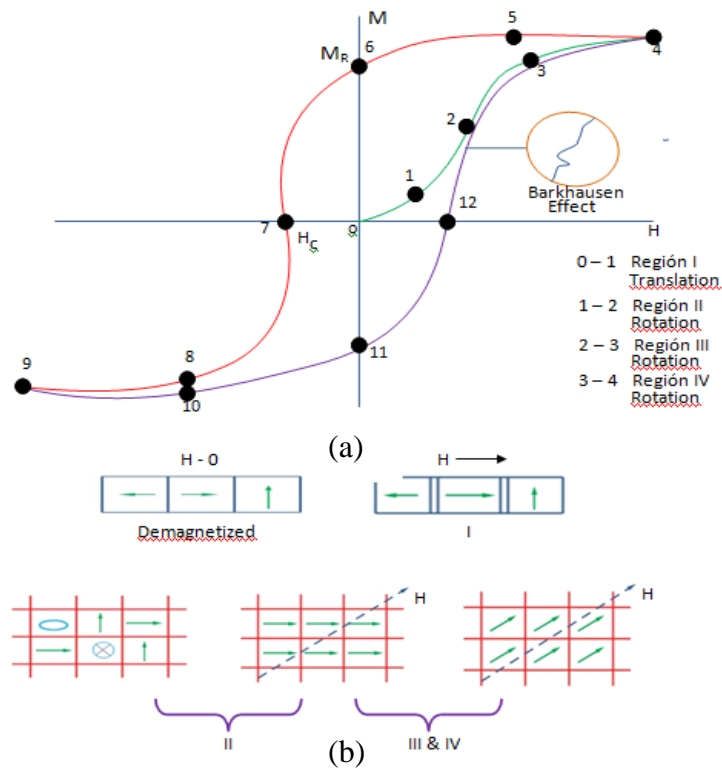
Figure 2.4 (a) The M-H hysteresis loop of a typical ferromagnetic material; (b) the magnetization processes in regions I, II, III, and IV [41].

area, which is given by

$$W_m = [\oint H dB] \qquad joules/m^3 - cycle \qquad (1)$$

when H is in ampere/m and B in Webers/m². The power loss is proportional to the frequency of the magnetization field. Thus, the total power loss, i.e., the total hysteresis energy loss per second, is

$$P = [\oint H dB] \, f \times (volume \ of \ the \ material) \qquad (2)$$

Where f is the frequency of the magnetic field. Note that the magnetic moment in one direction in one domain does not change abruptly to the reverse direction in a neighboring domain because of the exchange energy, which tends to keep the angle between adjacent magnetic moments small. Thus, the domain wall is a transitional region, enabling a gradual change in the spin direction, as shown in Figure 2.5. The domain wall width W_B that minimizes the total energy exchange energy and anisotropy energy is about 300 lattice constants (1000 A). The wall energy involved is about 10^{-7} joule cm^{-2} for a wall separating domains magnetized in opposite directions (a 180-degree wall). It can be imagined that the transition due to the motion of the domain walls can only be made with the expenditure of work. This constitutes the hysteresis loss for each cycle of an alternating magnetic field. In fact, hysteresis loss is a major component of power losses in electrical machines. To reduce this loss, we must use very soft magnetic materials with a very narrow M-H loop and also laminate the material in order to reduce the eddy current loss.
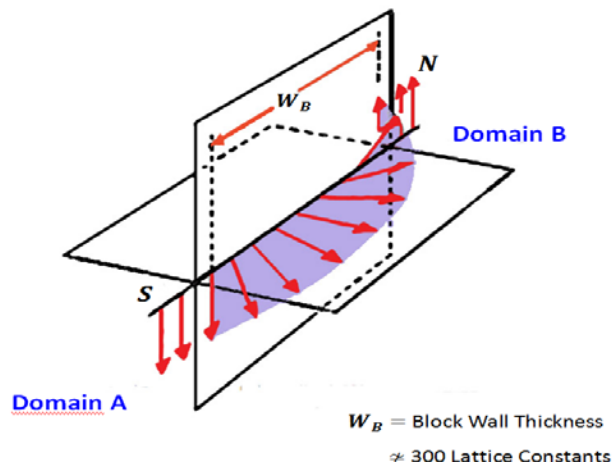
Figure 2.5 Gradual change of spin direction inside the domain wall [41].

2.3 Ferromagnetic Materials

In this section, I will discuss materials in which polarized magnetic dipole moments lead a material to show a net magnetization. The most well-known material that exhibits magnetic properties is the ferromagnet. For a ferromagnet, all magnetic dipoles in a domain are in parallel alignment. Even if all magnetic dipoles are not aligned, however, a net magnetic moment may still be observed. Such is the case with a ferrimagnet, a material in which the sum of the magnetic dipole moments in one direction is stronger than the net magnetic moment in the antiparallel direction [41]. The magnetic dipole orientations for both a ferromagnet and a ferrimagnet are depicted in Figure 2.6.
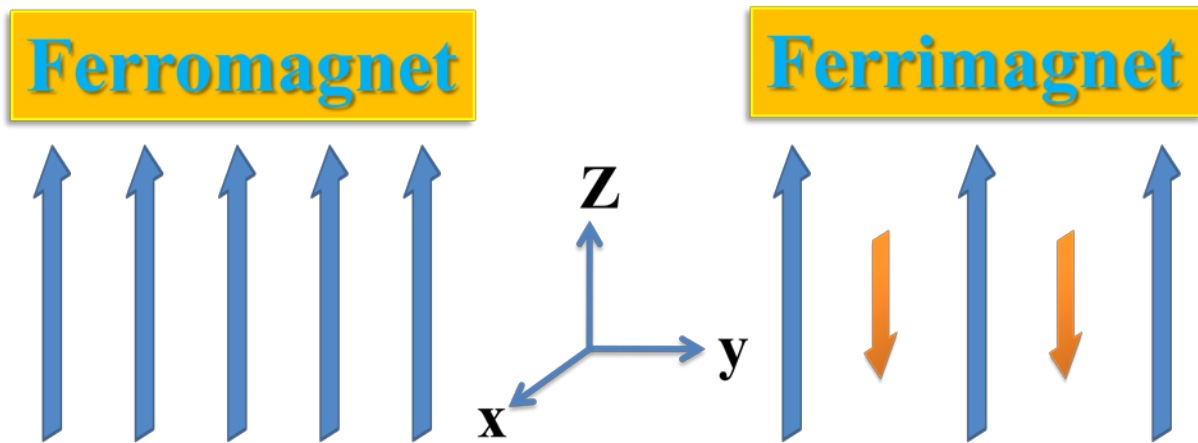
Figure 2.6 Magnetic dipole alignment for a ferromagnet and a ferrimagnet [42].

The magnetic dipole alignment of a ferrimagnet is a result of the material's crystal structure, which requires magnetic ions in the crystal lattice to assume an antiparallel spin configuration. This effect can be seen more clearly by considering the common ferrimagnet magnetite [$Fe^{3+}(Fe^{2+} Fe^{3+})O_4$], which has a perovskite crystal structure like that of $CoFe_2O_4$. The crystal lattice and ion spin orientation of magnetite is shown in Figure 2.7(a). The iron ions are positively charged (Fe^{3+}, Fe^{2+}) while the oxygen ions have a negative charge (O^{2-}). The close proximity of the Fe^{3+} ions to one another leads the orbitals to overlap. Pauli Exclusion Principle restricts the electrons from residing in the same spin state, and so the electrons assume an

antiparallel alignment [42]. Meanwhile, the Fe^{3+} and Fe^{2+} ions will maintain parallel spins due to a "double exchange" interaction that occurs between the two ions. Through this interaction, an electron effectively "jumps" from Fe^{3+} `to O^{2-}, resulting in Fe^{2+}. At the same time another electron "jumps" from O^{1-}, resulting in Fe^{2+}. This double exchange interaction is depicted in Figure 2.7(b). In order for exchange to occur, parallel spin configuration is required. The net magnetic moment of this material points upwards simply because more ion spins (and thus magnetic moments) are oriented in the upward direction [42].
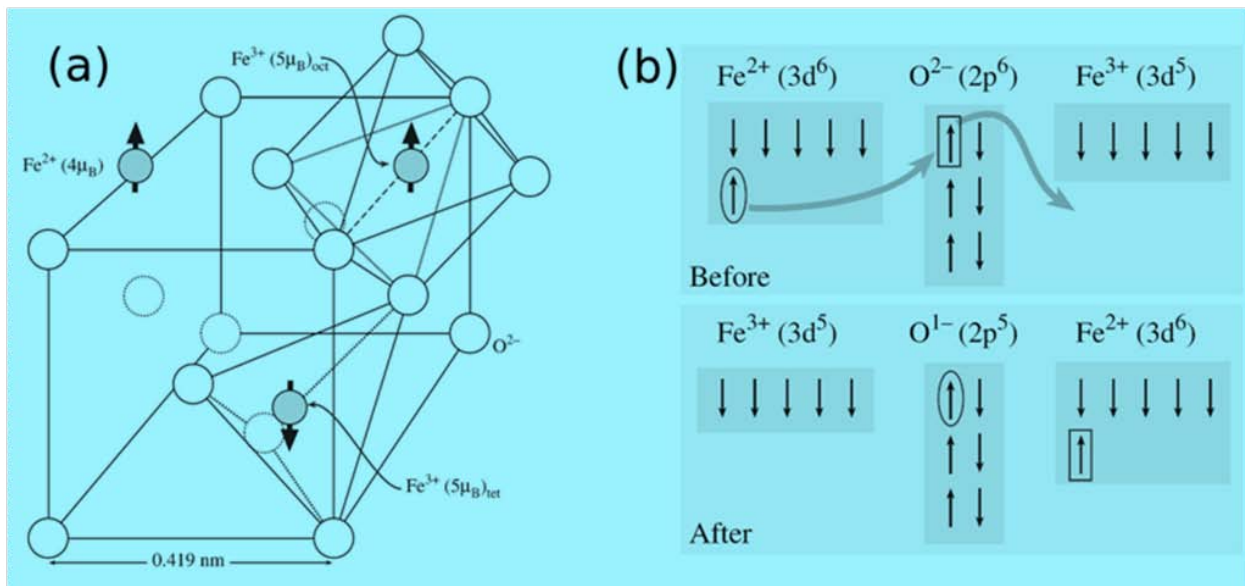
Figure 2.7 Ferrimagnetism exhibited by magnetite. (a) The orientation of the ion spins in the crystal lattice; (b) An illustration of the double exchange interaction which leads Fe^{3+} and Fe^{2+} to have parallel spin configuration. Images taken from [42].

Magnetic materials, exhibiting magnetic properties only up to a certain point, are also called the Curie temperature [42]. Above this critical temperature, the magnetic dipoles are reoriented from an ordered to a random fashion, resulting in no net magnetization.

2.4 Ferroelectric effect.

The polarization induced by an externally applied electric field, in normal dielectric materials, is very small with the dielectric constant usually less than 100 and its effects on other physical properties are also very small. However, there are a number of crystals with a nonsymmetrical structure (see Figure 2.8) that exhibit a large polarization, with the dielectric constant up to 10^5, under certain conditions. Obviously, such a large magnitude of polarization has attracted many researchers to study it theoretically and to develop various practical applications.
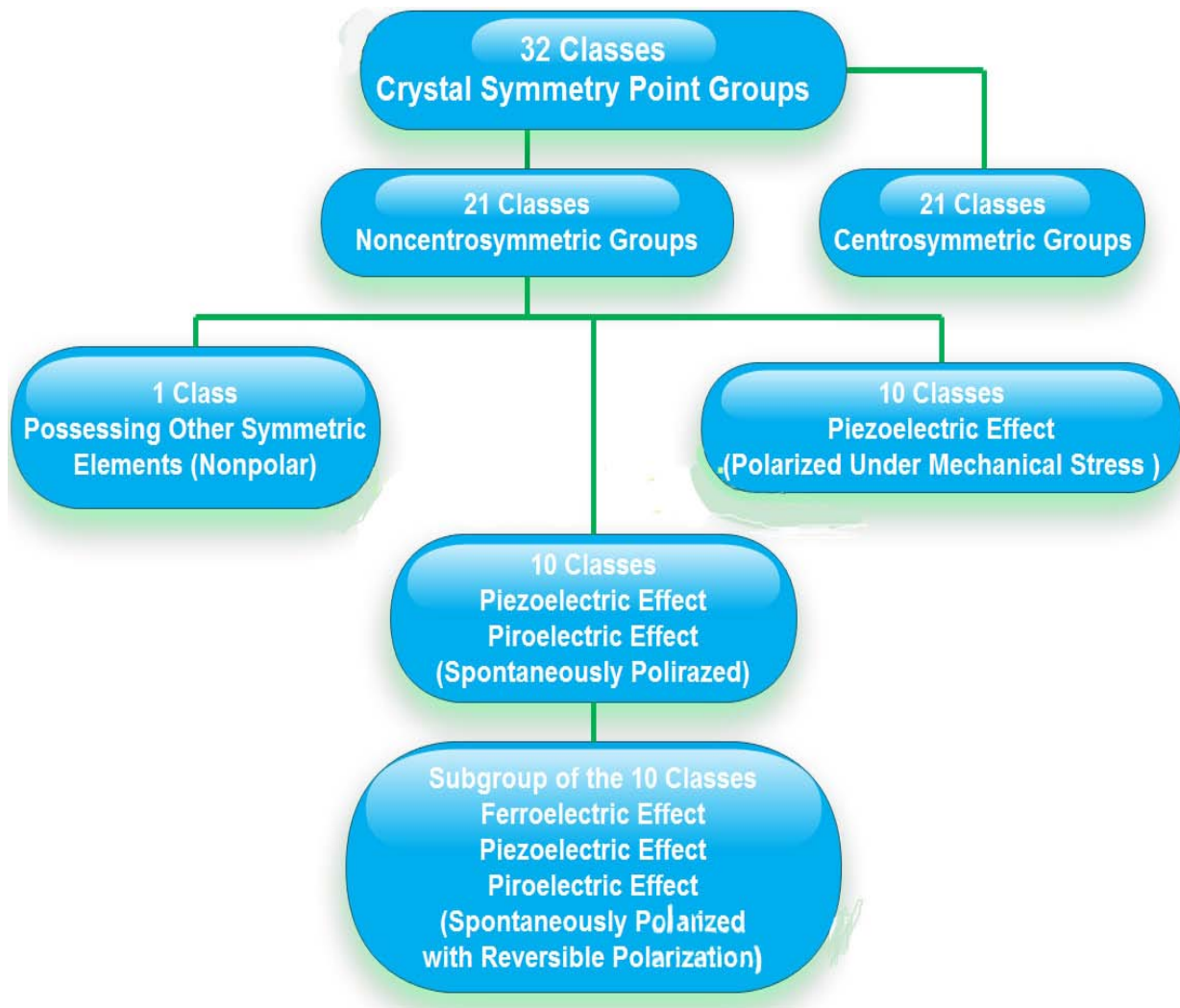
Figure 2.8 Classification of crystals showing the classes with piezoelectric, pyroelectric, and ferroelectric effects [41].

A ferroelectric crystal shows a reversible spontaneous electric polarization and a hysteresis loop that can be observed in certain temperature regions, delimited by a transition point called the Curie temperature, T_C. At temperatures above T_C, the crystal is no longer ferroelectric and exhibits normal dielectric behavior. Ferroelectric materials usually, but not always, exist in a nonpolar state at temperatures above T_C, and have anomalously high dielectric constants, especially near the Curie temperature. Typical dielectric constant temperature and polarization temperature characteristics are shown in Figure 2.9.
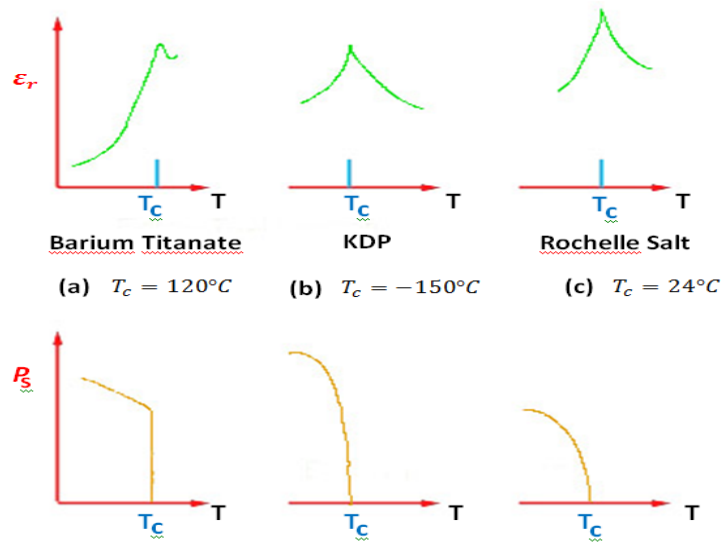
Figure 2.9 Schematic illustration of the variation of the dielectric constant ε_r and the spontaneous polarization of P_S with temperature for three typical ferroelectric crystals: (a) Barium titanate (BaTiO$_3$) with T_C = 120°C; (b) Potassium dihydrogen phosphate (KDP, KH$_2$PO$_4$) with T_C = -150°C, (c) Potassium Sodium tartrate-tetrahydrate (Rochelle Salt, KNaC$_4$H$_4$O$_6$.4H$_2$O) with T_C = 24°C [41].

The dielectric constant increases very rapidly to a very high peak value at T_C. The anomalously high value of ε_r in the neighborhood of T_C is generally referred to as the anomalous value. At $T > T_C$, anomalous behavior follows closely the Curie-Weiss relation:

$$\varepsilon_r = \frac{C}{T - T_C} \qquad (3)$$

where C is known as the Curie constant. In fact, anomalous behavior always appears near any transition point between two different phases, even at T below T_C. At the transition points, there are anomalies not only in the dielectric constant and polarization, but also in piezoelectric and elastic constants and specific heat, because of the change in crystal structure.

Ferroelectrics have reversible spontaneous polarization. The word spontaneous may mean that the polarization has a nonzero value in the absence of an applied electric field. The word reversible refers to the direction of the spontaneous polarization that can be reversed by an applied field in opposite direction [41]. The spontaneous polarization P_S usually increases rapidly on crossing the transition point, and then, gradually reaches a saturation value at lower temperatures. The most prominent features of ferroelectric properties are hysteresis and nonlinearity in the relation between the polarization P and the applied electric field E.

A typical hysteresis loop is shown schematically in Figure 2.10. When the field is small, the polarization increases linearly with the field. This is due mainly to field-induced polarization; because the field is not large enough to cause orientation of the domains (portion 0A). At fields higher than the low-field range, polarization increases nonlinearly with increasing field, because all domains start to orient toward the direction of the field (portion AB). At high fields, polarization will reach a state of saturation corresponding to portion BC, in which most domains are aligned toward the direction of the poling field. Now, if the field is gradually decreased to zero, the polarization will decrease, following the path CBD. By extrapolating the linear portion CB to the polarization axis (or zero-field axis) at E, 0E represents the spontaneous polarization P_s and 0D represents the remnant polarization P_r. The linear increase in polarization from P_s to P_p is due mainly to the normal field-induced dielectric polarization. P_r is smaller than P_s because when the field is reduced to zero, some domains may return to their original positions due to the strain situation, thus reducing these domains' contribution to the net polarization.
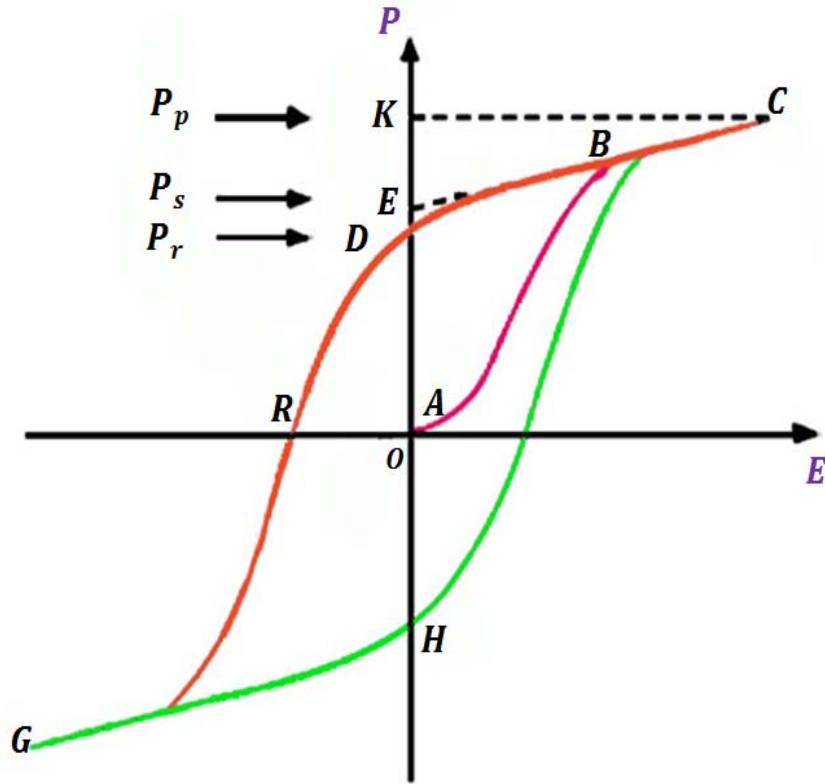
Figure 2.10. Schematic diagram of a typical ferroelectric hysteresis loop.

For most ferroelectric materials, the component due to the normal field-induced dielectric polarization is very small compared to the spontaneous polarization; therefore, for most applications, this component can be ignored. The magnitude of the difference between P_p and P_s in Figure 2-10 is exaggerated for the purpose of clear illustration. The field required to bring the polarization to zero is called the coercive field E_C (portion 0R on zero polarization axis) [41]. E_C depends not only on temperature, but also on the measuring frequency and the waveform of the applied field. When the field in the opposite direction decreases to zero, the polarization is reversed, indicating that domains have already been formed before poling and that the motion of the domain walls results in the change of direction of polarization. The hysteresis arises from the energy needed to reverse the metastable dipoles during each cycle of the applied field. The area of the loop represents the energy dissipated inside the specimen as heated during each cycle. In general, the hysteresis loop is measured with AC fields at low frequencies, 60 Hz or lower, to avoid heating the specimen.

In general, ferroelectricity is harder to demonstrate in polycrystalline materials composed of crystallites, such as ceramics, than in a single crystal because of the random orientation of crystallites. This is why in some single crystals the polarization reverses quite abruptly to form a square loop, as shown in Figure 2.11(a), while in most ceramics the loop is rounded, as shown in Figure 2.11(b), because of the more sluggish reversal, which is due partly to the axes of the unit cells in the randomized arrangement of the nonuniform crystallites.

(a)   (b)
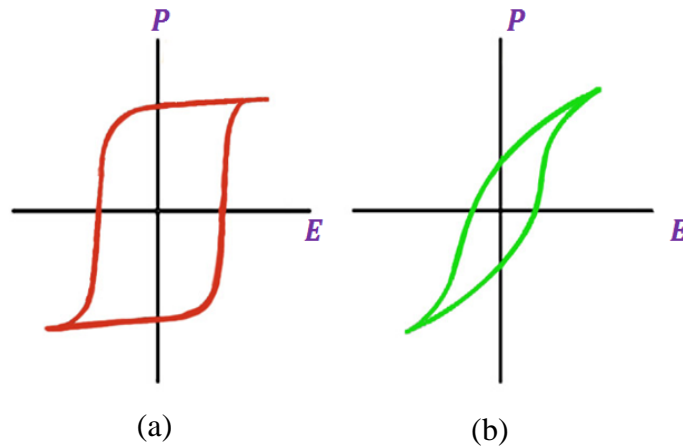
Figure 2.11   Schematic diagrams of (a) the "square"; (b) the "rounded" hysteresis loops [41].

Ferroelectric materials exhibit ferroelectric properties only at temperatures below T_C because they are polar at temperatures above it, they are not polar. Obviously, the shape of the hysteresis loop depends on temperature. Figure 2.12 shows the shape of the hysteresis loop for Rochelle salt at two different temperatures. The loop becomes gradually diminished at $T > T_C$, eventually degenerating to a straight line at T much larger than T_C, when the ferroelectric behavior disappears completely. However, some ferroelectric materials can be driven from the paraelectric state to a ferroelectric state at $T > T_C$ by an applied field larger than a certain critical value E_t. In other words, the applied electric field larger than F_t tends to shift the Curie point to a higher temperature. The higher the temperature above T_C, the higher the field required to induce ferroelectricity.
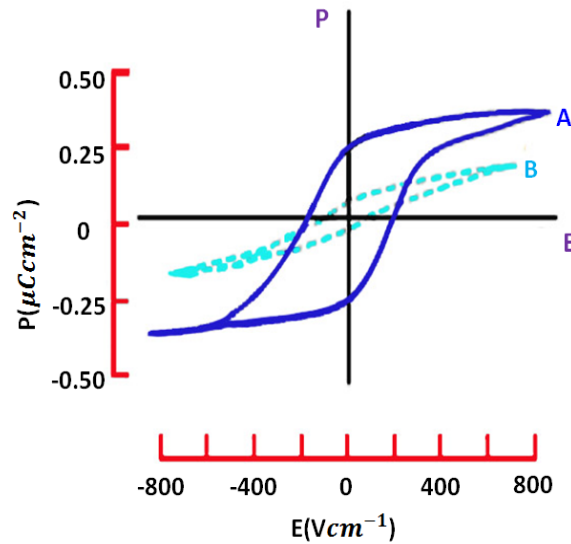
Figure 2.12 Temperature dependence of the hysteresis loop for Rochelle salt with T_C = 24°C. (A) T = 19°C < T_C, and (B) T = 42°C > T_C [41].

If a ferroelectric material is subjected to a large AC field at a temperature slightly higher than T_C, two small hysteresis loops may appear, as shown schematically in Figure 2.13. A double hysteresis loop has been observed in $BaTiO_3$ at a temperature a few degrees above T_C [43-44]. For the transition from the tetragonal structure to the orthorhombic structure at the transition temperature of 5°C for $BaTiO_3$ at an AC field higher than E_t, a triple hysteresis loop consisting of one main loop and two small loops, has also been observed [45]. Using the circuit shown in Figure 4.3, the voltage across *C* is proportional to the polarization P, which is the dipole moments per unit volume and is also equal to the surface charge density on the electrode. During polarization, a current j = dP/dt will flow through the specimen per unit area.

Suppose that the wave shape of the switching signal voltage is as shown in Figure 2.14(a) for two cases: one with the voltage (or field) increasing linearly with time and the other with the field decreasing linearly with time. In this case, the resulting current flowing through the specimen, for a normal linear dielectric, is constant, as shown in Figure 2.14(b). But if the specimen is a ferroelectric material, the current will be a short pulse, as shown in Figure 2.14(c). This is one of the simplest ways to distinguish ferroelectric from nonferroelectric materials.

The size of the unit cell and the force of ions in the lattice of a crystal are temperature dependent. As the temperature changes, there exists a critical temperature (i.e., the transition

temperature), at which a particular structure becomes unstable and tends to transform to a more stable one. Although the transition involves only small ionic movements, they cause a marked change in properties. A change in dimensions of a crystal or a crystallite will create internal stresses, particularly at the boundaries between crystallites in polycrystalline materials, such as in ceramics. Under certain conditions, the magnitude of such stresses may be large enough to cause internal cracks. Transition from one crystal structure to another usually involves a change in entropy and volume. In general, there are two different orders of transition. When the spontaneous polarization goes from zero to a finite value, or from one value to another, the change in polarization may be continuous or discontinuous. If there is discontinuity in the change of the polarization, the transition is referred to as a first order transition, as in $BaTiO_3$, as shown in the Figure 2.15(a) and (c) [45]. In this case, the entropy changes at a constant temperature (e.g., $T = T_C$), and consequently the latent heat also changes. If the change of the polarization is continuous, the transition is referred to as a second-order transition, as in KH_2PO_4 and Rochelle salt. As shown in the Figure 2.15(b) and (d) [45]. In this case, there is no change in entropy and latent heat at the transition temperature. It is interesting to note that at the Curie temperature, the transition in ferromagnetic materials does not involve changes in crystal structure but only a small change in the coupling forces between the outer electrons of neighboring magnetic ions. Since the dielectric constant of ferroelectric materials is extremely high near the transition temperature, the polarization induced in the paraelectric (nonpolar) region at $T > T_C$ by an applied electric field along the ferroelectric axis goes gradually over into the spontaneous polarization region upon cooling below T_C.
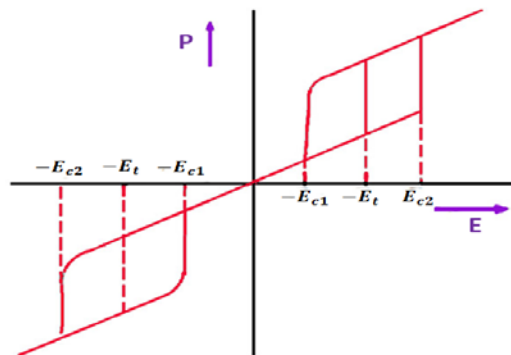
Figure 2.13   Schematic diagram showing a typical double hysteresis loop at T slightly higher than T_C and at E larger than a critical value E_t.
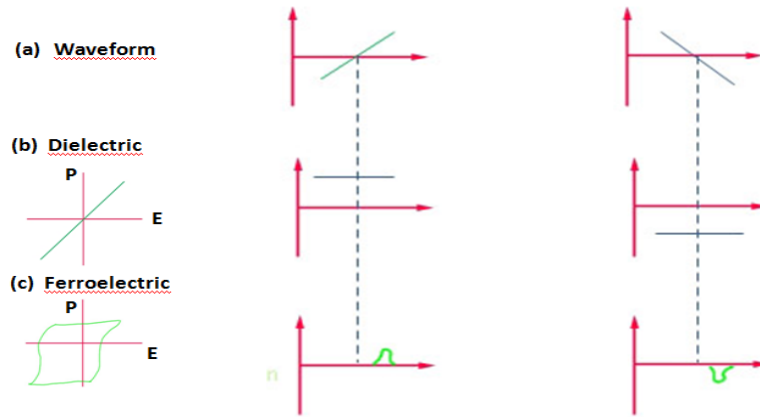
Figure 2.14 Schematic diagrams showing (a) the waveforms of the linearly time-varying electric field; (b) the corresponding current j flowing through the loss-free dielectric material; (c) the corresponding current j flowing through the ferroelectric material [41].

The effect of this field tends to shift T_C to a higher temperature, as shown in Figure 2.15. The polarization-temperature curve shifts to a higher temperature as the applied field is increased. However, the concept of the Curie temperature cannot be applied to ferroelectric materials under the electrically biased condition [44, 46]. In general, if the direction of the applied field is parallel to the polar direction of any phase, it favors the existence of that phase and extends its temperature range. At T_C, the ferroelectric phase is favored by an applied field; therefore, the Curie temperature is raised. A change in crystal structure and crystal volume caused by any external forces, such as electric fields, mechanical stresses, or hydrostatic pressures, will affect the phase transition. A shear stress is essentially equivalent to an electric field along the ferroelectric axis and therefore would have a similar effect on the polarization-temperature curve, as shown in Figure 2.15. It should be noted that in Equation 3, the Curie temperature T_C coincides with the actual transition temperature at which spontaneous polarization begins to rise if the transition is of the second order. For first-order transitions, T_C is generally slightly lower than the actual transition temperature by several degrees (typically ~10 K) [46]. Because the difference is very small, and for general uses, T_C is usually considered the actual transition temperature. When the temperature decreases through T_C, the polarization rises from zero continuously over several degrees of temperature if the transition is of the second order. However, when the polarization rises abruptly from zero at T_C following the first-order transition, then the rise involves a change of the latent heat, implying that the process is

equivalent to supercooling. When the temperature is reversed that is, increases through the transition point the process becomes superheating, and a collective or cooperative action among the dipoles and surrounding ions tends to hold the spontaneous polarization until a slightly higher temperature is reached, as shown in Figure 2.15(c). A similar phenomenon occurs at any transition point if the transition is of the first order. But this phenomenon does not occur if the transition is of the second order, as shown in Figure 2.15(d).
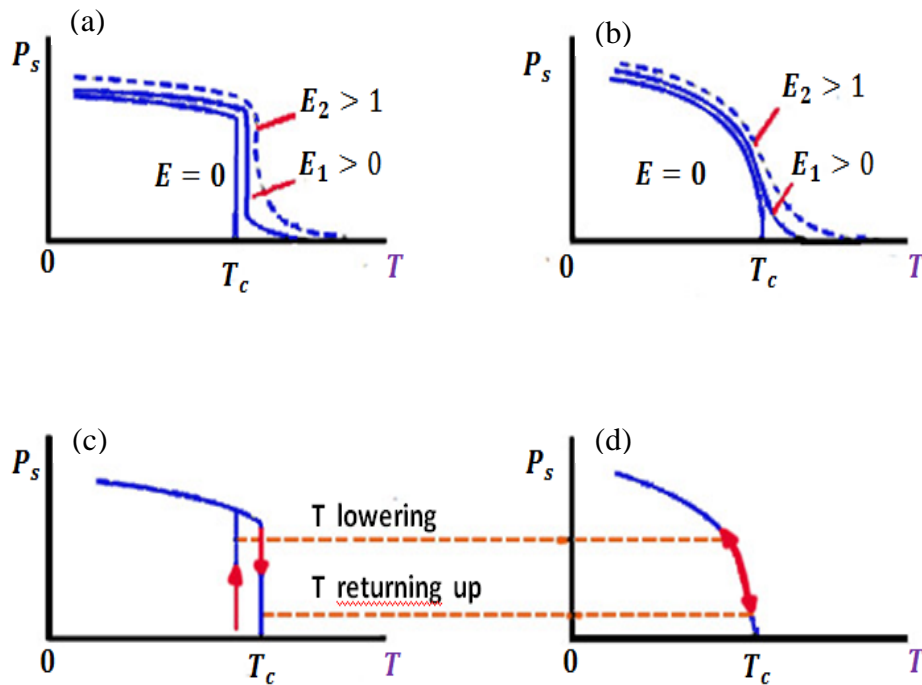
Figure 2.15 Schematic diagrams illustrating the effect of applied electric field on (a) first order transition; (b) second order transition, and the shift of the transition point when the temperature is returning up (increasing); (c) T_C shifts to a higher temperature for the first order transition, and (d) there is no shift for the second order transition [41].

2.5 Ferroelectric Materials

A material is said to be ferroelectric when it exhibits an intrinsic electric polarization in the absence of an electric field [47]. Such polarization can be clearly illustrated by looking at the crystal lattice structure of certain types of ferroelectric materials. For example, the ferroelectric effect is often observed in the case of materials having a perovskite lattice structure [47]. This crystal structure is depicted in Figure 2.16(a) and (b). The atoms represented by blue and orange spheres are generally positively-charged cations. The red atoms are most commonly oxygen ions with a negative charge. The negatively charged oxygen ions exert an electrostatic force on the positive cations, causing distortion of the crystal structure, as shown in Figure 2.16(c). The arrows depict the stretching motion due to the electrostatic force. The result is the electrically polarized material, as shown in Figure 2.16(d).
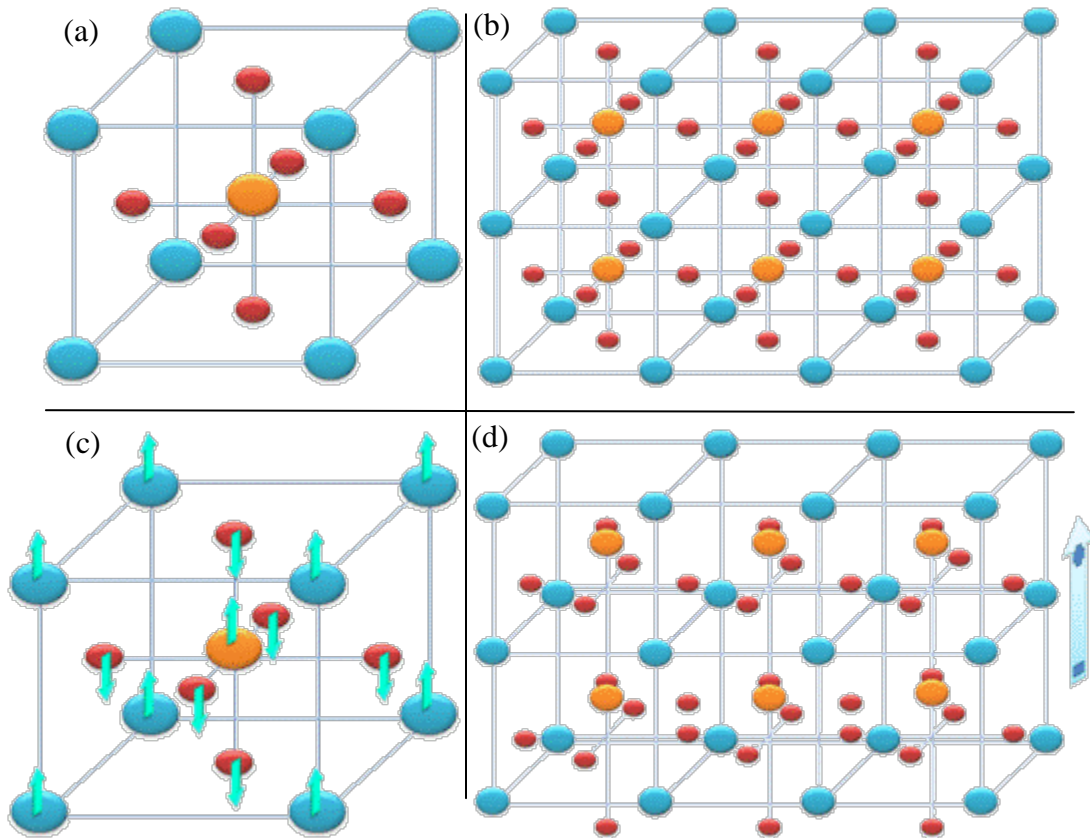
Figure 2.16 Schematic of the ferroelectric effect for a perovskite. (a) A perovskite unit cell; (b) A perovskite lattice; (c) Crystal structure distortion due to electrostatic forces between the ions; (d) Resulting electric polarization of the crystal [42].

The ferroelectricity of a material also depends on temperature [47]. Above a certain temperature, called the ferroelectric Curie temperature, the polarized structure of the crystal lattice becomes energetically unfavorable, and a transition from a ferroelectric to nonferroelectric state occurs. In the case of a common ferroelectric, $BaTiO_3$, the Curie temperature T_C is 135^0C [47]. For $BiFe_3O_4$, the ferroelectric used in this experiment, the Curie temperature is significantly higher, roughly 400^0C. BFO/$BaTiO_3$ composite, thin films have shown ferroelectric polarization [48]. Multiferroic materials with their co-existing ordered states of electric and magnetic dipoles may find use in many technological applications, such as magnetoelectric random - access memory.

In some cases, external conditions lead certain materials to exhibit spontaneous polarization. For example, pyroelectrics such as $PbTiO_3$ will gain internal electric dipole moments when the material is subjected to heat. As temperature rises, the dielectric constant of the material gradually increases until, at a critical temperature, it reaches a maximum. Beyond this temperature, the material is no longer ferroelectric because the temperature exceeds the Curie temperature of the material [47]. All ferroelectrics exhibit electric polarization when the material is subjected to stress or strain. This is called the piezoelectric effect [47].

2.6 Piezoelectric Effect

The piezoelectric effect is a phenomenon where by mechanical stress or strain leads to reorientation of electric dipoles through a material, inducing a spontaneous change in the charge polarization [49]. All ferroelectrics exhibit the piezoelectric effect (although all piezoelectrics are not necessarily ferroelectrics). The piezoelectric effect may be formally described by the following set of equations, which provide a relationship between the electric displacement D, the electric field E, and the stress and strain, T and S, respectively [49]:

$$D = \epsilon_T E + d_{33} T \qquad (4)$$

$$S = d_{33} E + s_E T \qquad (5)$$

where ϵ_T is the dielectric constant and d_{33} is the piezoelectric constant. s_E is the material's compliance in the presence of a constant electric field. This constant s_E, describes the stress strain relationship for a material and is based on the material's Young's modulus and Poisson's ratio [50]. From the equations above, it can be seen that any increase or decrease in stress (T) or strain (S) on the material will lead to an increase or decrease in electric displacement (D) and in the material's electric field (E). These relations also predict the existence of the converse piezoelectric effect, whereby a piezoelectric material physically changes shape when an external electric field E is introduced. This altered shape is a result of an increase in stress T and strain S on the material due to the electric field change. The piezoelectric effect is used in a variety of applications because the crystal motion resulting from the electric field is both predictable and precise. Common piezoelectrics include Lead-Zirconate-Titanate (PZT) and bismuth ferrite [49]. Figures 2.16(a) and (b) provide a schematic representation of the piezoelectric effect. The blue spheres in these figures denote positively-charged ions while the pink spheres denote negatively charged ions. Due to its lattice structure, the material has an intrinsic polarization Po in its initial state, as shown in Figure 2.16(a). In Figure 2.16(b), the material is subject to mechanical stress. The charge distribution within the material is altered, leading to a new polarization P_f:

$$P_f = P_0 + \Delta P \qquad (6)$$

Figures 2.15(c) and (d) demonstrate the converse piezoelectric effect. The external electric field represented by green arrows leads the ions in the material to shift: the positively-charged ions move in the positive z-direction while the negatively-charged ions move in the opposite direction. The result is a distortion of the physical shape of the piezocrystal:

$$x_f, y_f, z_f = x_0, y_0, z_0 + \Delta x, \Delta y, \Delta z \qquad (7)$$

As noted before, a material need not be ferroelectric in order to demonstrate the piezoelectric effect. The dipole moments of a material may be in equilibrium until stress or strain disrupts this equilibrium, leading to non-zero electric polarization. Such is the case for the common piezoelectric quartz. While this is an interesting phenomenon, it will not be discussed in great detail here, as $BiFeO_3$ is a ferroelectric piezoelectric. It is also worth noting that, as is the case

26

for all ferroelectrics, the piezoelectric effect can only be observed for materials below the ferroelectric Curie temperature since above this temperature, the net electric polarization is zero.
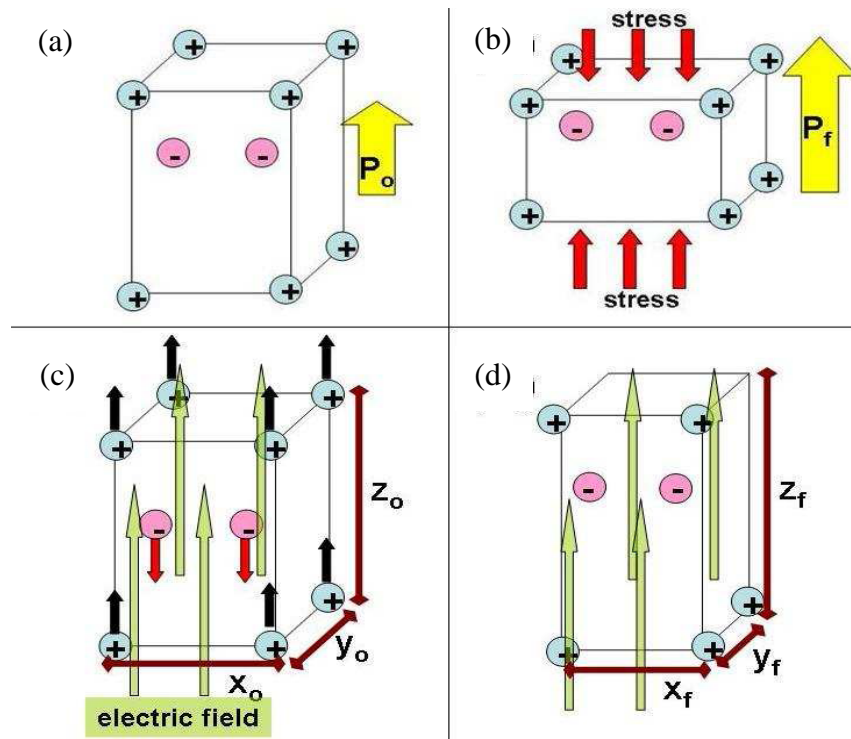
Figure 2.17   A schematic of the piezoelectric effect, (a) and (b), and the inverse piezoelectric effect, (c) and (d). (a) Intrinsic electric polarization of the material prior to applied stress; (b) Applied stress causes the electric polarization strength to change; (c) An external electric field is applied to a piezoelectric, causing the ions to shift; (d) The shape of the crystal is altered due to the movement of ions.

2.7 Multiferroics

Multiferroics describes materials in which two or all three of the properties ferroelectricity, ferromagnetism, and ferroelasticity, occur in the same phase [51, 52]. The overlap required of ferroic materials to be classified as multiferroic is shown schematically in Figure 2.18 (a). Only small subgroups of all magnetically and electrically polarizable materials are either ferromagnetic or ferroelectric, and fewer still simultaneously exhibit both order parameters. In these selected materials, however, there is a possibility that electric fields cannot

only reorient the polarization but also control magnetization; similarly, a magnetic field can change electric polarization. This functionality offers an extra degree of freedom and hence we refer to such materials as magnetoelectrics, as shown in Figure 2.18 (b).

Magnetoelectricity is an independent phenomenon that can arise in any material with both magnetic and electronic polarizability, regardless of whether it is multiferroic or not. By definition, a magnetoelectric multiferroic must be simultaneously both ferromagnetic and ferroelectric [53]. It should be noted, however, that the current trend is to extend the definition of multiferroics to include materials possessing two or more of any of the ferroic or corresponding antiferroic properties such as antiferroelectricity and antiferromagnetism. The scarcity of magnetoelectric multiferroics can be understood by investigating a number of factors including symmetry, electronic properties, and chemistry. We note that there are only 13 point groups that can give rise to multiferroic behavior.

Additionally, ferroelectrics by definition are insulators (and in 3d transition metal based oxides, typically possess ions that have a formal d^0 electronic state), while itinerant ferromagnets need conduction electrons; even in double exchange ferromagnets such as the manganites, magnetism is mediated by incompletely filled 3d shells. Thus, there exists a seeming contradiction between the conventional mechanism of off-centering in a ferroelectric and the formation of magnetic order which explains the scarcity of ferromagnetic-ferroelectric multiferroics [54]. The focus of many researchers, in turn, has been in designing and identifying new mechanisms that lead to magnetoelectric coupling and multiferroic behavior. It has been proposed that one can engineer multiferroic properties by chemically controlling the functionality on a site by site basis. Many researchers have focused on model systems, such as the perovskites with chemical formula ABO_3, as a pathway for the creation of multiferroic behavior. Single phase multiferroism has been identified in only a few perovskite oxides and is typically achieved by making use of the stereochemical activity of the lone pair on large (A site) cations to provide ferroelectricity while retaining magnetism on the smaller (B site) cations. This is the case in one of the most widely studied single phase multiferroics the antiferromagnetic, ferroelectric $BiFeO_3$ [15].
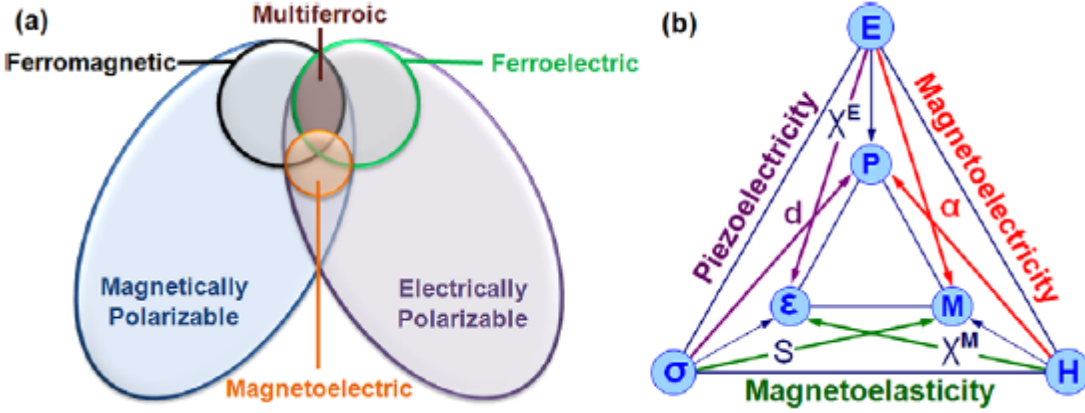
Figure 2.18 (a) Relationship between multiferroic and magnetoelectric materials. Illustrate the requirements to achieve both in a material; (b) Schematic illustrating different types of coupling present in materials. Much attention has been given to materials where electric and magnetic order is coupled. These materials are known as magnetoelectric materials [55].

2.7.1 Magnetoelectric coupling

The magnetoelectric effect in a single-phase crystal is traditionally described in Landau theory by writing the free energy F of the system in terms of an applied magnetic field H whose ith component is denoted H_i, and an applied electric field E whose ith component is denoted E_i [56]. Note that this convention is unambiguous in free space, but that E_i within a material encodes the resultant field that a test particle would experience. Let us to consider a non-ferroic material, where both the temperature-dependent electrical polarization $P_i(T)$ (μCcm^{-2}) and the magnetization $M_i(T)$ (μ_B per formula unit, where μ_B is the Bohr magneton) are zero in the absence of applied fields and there is no hysteresis. It may be represented as an infinite, homogeneous and stress-free medium by writing F under the Einstein summation convention in S.I. units as:

$$-F(\vec{E}, \vec{H}) = \frac{1}{2}\varepsilon_0\varepsilon_{ij}E_iE_j + \frac{1}{2}\mu_0\mu_{ij}H_iH_j + \alpha_{ij}E_iH_j + \frac{\beta_{ijk}}{2}E_iH_jH_k + \frac{\gamma_{ijk}}{2}H_iE_jE_k + \cdots \qquad (8)$$

The first term on the right hand side describes the contribution resulting from the electrical response to an electric field, where the permittivity of free space is denoted ε_0, and the

relative permittivity $\varepsilon_{ij}(T)$ is a second-rank tensor that is typically independent of E_i in non-ferroic materials. The second term is the magnetic equivalent of the first term, where $\mu_{ij}(T)$ is the relative permeability and μ_0 is the permeability of free space. The third term describes linear magnetoelectric coupling via $\alpha_{ij}(T)$; the third-rank tensors $\beta_{ijk}(T)$ and $\gamma_{ijk}(T)$ represent higher-order (quadratic) magnetoelectric coefficients. In the present scheme, all magnetoelectric coefficients incorporate the field independent material response functions $\varepsilon_{ij}(T)$ and $\mu_{ij}(T)$. The magnetoelectric effects can then easily be established in the form $P_i(H_j)$ or $M_i(E_j)$. The former is obtained by differentiating F with respect to E_i, and then setting $E_i=0$. One obtains the polarization:

$$P_i(\vec{E},\vec{H}) = -\frac{\partial F}{\partial E_i} = \varepsilon_0\varepsilon_{ij}E_j + \alpha_{ij}H_j + \frac{\beta_{ijk}}{2}H_jH_k + \gamma_{ijk}H_jE_k + \cdots \tag{9}$$

$$P_i(\vec{H}) = \alpha_{ij}H_j + \frac{\beta_{ijk}}{2}H_jH_k + \cdots \tag{10}$$

The former is obtained by differentiating F with respect to H_i, and then setting $H_i=0$. One obtains the magnetization:

$$M_i(\vec{E},\vec{H}) = -\frac{\partial F}{\partial H_i} = \mu_0\mu_{ij}H_j + \alpha_{ij}E_j + \beta_{ijk}E_jH_k + \frac{1}{2}\gamma_{ijk}E_jE_k + \cdots \tag{11}$$

$$M_i(\vec{E}) = \alpha_{ji}E_j + \frac{\gamma_{ijk}}{2}E_jE_k + \cdots \tag{12}$$

In ferroic materials, the above analysis is less rigorous because $\varepsilon_{ij}(T)$ and $\mu_{ij}(T)$ display field hysteresis. Moreover, ferroics are better parameterized in terms of resultant rather than applied fields [57]. This is because it is then possible to account for the potentially significant depolarizing/demagnetizing factors infinite media, and also because the coupling constants would then be functions of temperature alone, as in standard Landau theory. In practice, resultant electric and magnetic fields may sometimes be approximated [58] by the polarization and magnetization respectively.

A multiferroic that is ferromagnetic and ferroelectric, is liable to display large linear magnetoelectric effects. This follows because ferroelectric and ferromagnetic materials often (but not always) possess a large permittivity and permeability respectively, and $\alpha_{ij}(T)$ is bounded by the geometric mean of the diagonalized tensors $\varepsilon_{ii}(T)$ and $\mu_{jj}(T)$such that [59]:

$$\alpha_{ij}^2 \leq \varepsilon_0\mu_0\varepsilon_{ii}\mu_{jj} \tag{13}$$

Equation (13) is obtained from equation (8) by forcing the sum of the first three terms to be greater than zero, that is, ignoring higher-order coupling terms. It represents a stability condition on $\varepsilon_{ij}(T)$ and $\mu_{ij}(T)$, but if the coupling becomes so strong that it drives a phase transition to a more stable state, then $\alpha_{ij}(T)$, $\varepsilon_{ij}(T)$ and $\mu_{ij}(T)$ take on new values in the new phase. Note that a large $\varepsilon_{ij}(T)$ is not a prerequisite for a material to be ferroelectric (or vice versa); and similarly ferromagnets do not necessarily possess large $\mu_{ij}(T)$. For example, the ferroelectric KNO_3 possesses a small $\varepsilon = 25$ near its Curie temperature of 120^0 C [60], whereas paraelectric $SrTiO_3$ exhibits $\varepsilon < 50,000$ at low temperatures [61]. Therefore large magnetoelectric couplings need not arise in, or be restricted to, multiferroic materials.

2.7.2 Nonlinear coupling

Most materials have small values of either $\varepsilon_{ij}(T)$ or $\mu_{ij}(T)$ or both, so the linear magnetoelectric effect will also be small, given that permittivity and permeability appear as a product in equation (6). However, no such restriction applies to higher-order couplings, such as those described by $\beta_{ijk}(T)$ and $\gamma_{ijk}(T)$. For example, in some materials terms such as $\beta_{ijk}H_jH_k$ can dominate the linear term $\alpha_{ij}H_j$ in equation (10), as first shown experimentally at low temperatures in the piezoelectric paramagnet $NiSO_4.6H_2O$ [62]. In order to achieve large magnetoelectric effects at room temperature through higher-order terms, we suggest investigating magnetic materials with reduced dimensionality. Indeed, two-dimensional spin order associated with $\beta(T)$ can persist to a temperature T_{2D} that exceeds the temperature T_{3D} at which three-dimensional spin order associated with $\alpha(T)$ is destroyed. This scenario arises at low temperature in $BaMnF_4$ [63].

2.7.3 Indirect coupling

So far, our discussion of linear and higher-order magnetoelectric coupling has ignored the effects of strain. Such effects could be significant or even dominant. For example, the inclusion of piezomagnetism (magnetostriction) would generate cross terms in equation (8) that are proportional to strain and vary linearly (quadratically) with H_i. Analogous expressions would arise from piezoelectricity or electrostriction. Furthermore, mixed terms involving products of strain, H_i and E_j have been predicted [64]. In two-phase materials, magnetic and electrical properties are strain-coupled by design in the quest for large magnetoelectric effects. The strength of this indirect coupling is not restricted by equation (13), and enhancements over single-phase systems of several orders of magnitude have been achieved [65].

The best example of this class of multiferroic is probably $BiFeO_3$ (BFO). This is perhaps the only material that is both magnetic and a strong ferroelectric at room temperature, making it the preferred model system for fundamental and theoretical studies of multiferroics. In BFO, the magnetism is associated with the 3d electrons of the Fe^{3+} cations. The ferroelectricty arises from the hybridization between the oxygen 2p orbitals and the empty Bi 6p orbitals, which are low lying in the conduction band and spatially extended due to the presence of the so-called lone-pair $6s^2$ electrons. A recently observed electric field induced spin flop in BFO single crystals demonstrates that the antiferromagnetic and ferroelectric order parameters in BFO are coupled [54]. It has been argued that the magneto-electric coupling in BFO is intimately related to the presence of a magnetic cycloid structure that allows a coupling of M and P on an atomic level even in antiferromagnetic structures where on average the linear ME-effect is forbidden. In geometric multiferroics, the ferroelectric instability has its origin in the topology of the chemical structure, and the ferroelectric distortions are driven by ionic size effects.

3. MOTIVATION AND GOALS

In order to have a possible coupling at room temperature, we look at $BiFeO_3$ substituted by a magnetic ion on Fe-ion site for a possible and effective multi-ferroic material and to investigate such materials in details for their structural, magnetic and electrical polarization. The idea here is to create a composite material system with alternate ferromagnetic and ferroelectric layers of material in the same phase [66]. It could have strains in the system, and might affect the coupling parameters. There seems to be a very small region for such possibility [67].

The goal was to study these materials for possible co-existence of ferromagnetic and ferroelectric coupling at room temperature. We have utilized a simple sol-gel process for the preparation the solution, after is grown the thin films by spin-coating. Such less expensive technique could be useful for reliable multifunction devices, if effective ferroelectric and ferromagnetic effect could be achieved with this technique.

4. EXPERIMENTAL PROCEDURE

4.1 Solutions preparation.

The Sol-Gel approach was used to synthesize targeted materials. Bismuth (III) nitrate pentahydrate, (CAS 10035-06-0) [Bi(NO$_3$)$_3$.5H$_2$O] (98%, Aldrich), Iron (III) nitrate nonahydrate, (CAS 7782-61-8) [Fe(NO$_3$)$_3$.9H$_2$O] (98%, Aldrich), Cobalt (II) nitrate hexahydrate, (CAS 10026-22-9) [Co(NO$_3$).6H$_2$O] (98%, Aldrich), Chromium (III) nitrate nonahydrate, (CAS 7789-02-8) [Cr(NO$_3$)$_3$.9H$_2$O] (99%, Aldrich), Manganese (III) acetylacetonate, (CAS 14284-89-0) [Mn(CH$_3$COCHCOCH$_3$)$_3$] (97%, Strem Chemicals) were used as precursor salts. 2-methoxyethanol was used as a solvent. To achieve specific compositions in the solid phase of the salt BiFe$_{1-x}$D$_x$O3, the following formula was used:

$$A = \left(\frac{0.07 \; mol \; Bi}{L}\right)(10 \times 10^{-3}L)\left(\frac{1mol \; Bi_{nitrate}}{1mol \; Bi}\right)(F.W.Bi)\left(\frac{98}{100}\right) \tag{14}$$

$$B = (1-x)\left(\frac{0.07 \; mol \; Fe}{L}\right)(10 \times 10^{-3}L)\left(\frac{1mol \; Fe_{nitrate}}{1mol \; Fe}\right)(F.W.Fe)\left(\frac{98}{100}\right) \tag{15}$$

$$C = x\left(\frac{0.07 \; mol \; D}{L}\right)(10 \times 10^{-3}L)\left(\frac{1mol \; D_{nitrate}}{1mol \; D}\right)(F.W.D)\left(\frac{98}{100}\right) \tag{16}$$

Where A, B and C are the amounts in grams of Bi, Fe and D= (Co, Cr and Mn), respectively.

In the next step, Bismuth (III) nitrate pentahydrate, (CAS 10035-06-0) [Bi(NO$_3$)$_3$.5H$_2$O] (98%, Aldrich), Iron (III) nitrate nonahydrate, (CAS 7782-61-8) [Fe(NO$_3$)$_3$.9H$_2$O] (98%, Aldrich), Cobalt (II) nitrate hexahydrate, (CAS 10026-22-9) [Co(NO$_3$).6H$_2$O] (98%, Aldrich), Chromium (III) nitrate nonahydrate, (CAS 7789-02-8) [Cr(NO$_3$)$_3$.9H$_2$O] (99%, Aldrich), Manganese (III) acetylacetonate, (CAS 14284-89-0) [Mn(CH$_3$COCHCOCH$_3$)$_3$] (97%, Strem Chemicals) were dissolved in 10.0 ml of 2-methoxyethanol under room temperature conditions. The solution was placed in ultrasonic bath during approximately 50 minutes; the organic salts were fully dissolved, which served as the coating solution. The total volume of this solution was

10.0 ml with a final concentration of 0.07 mol/L. This value is similar at the reference [84]. The solutions were deposited by spin coating onto platinum pieces (0.8×0.8 cm^2) substrate by spin coating.

4.2 Thin film preparation.

Substrates Pt/Ti/SiO$_2$/Si were cleaned with distilled water and acetone (ACS grade; 99.5%, CH$_3$COCH$_3$), and dried in a furnace at 300°C for 10 minutes. This cleaning process favored the adherence of the deposited film on the substrate.

After setting the substrate on the disk of the spin coater, the coating solution was added dropwise while spin coating at a speed of 5000 rpm for 30 s in air. The precursor film was placed onto a hot plate (in air) for 5 minutes at 300°C in order to remove residues of solvent. The dried film was then placed back onto the spin coater to repeat the previous coating process. This coating/drying cycle was repeated 30 times to build up the desired thickness. Produced films were heated (annealed) in air at 525°C for 1 hour in air atmosphere. Figure 4.1 summarizes the steps followed in the preparation of the thin films.
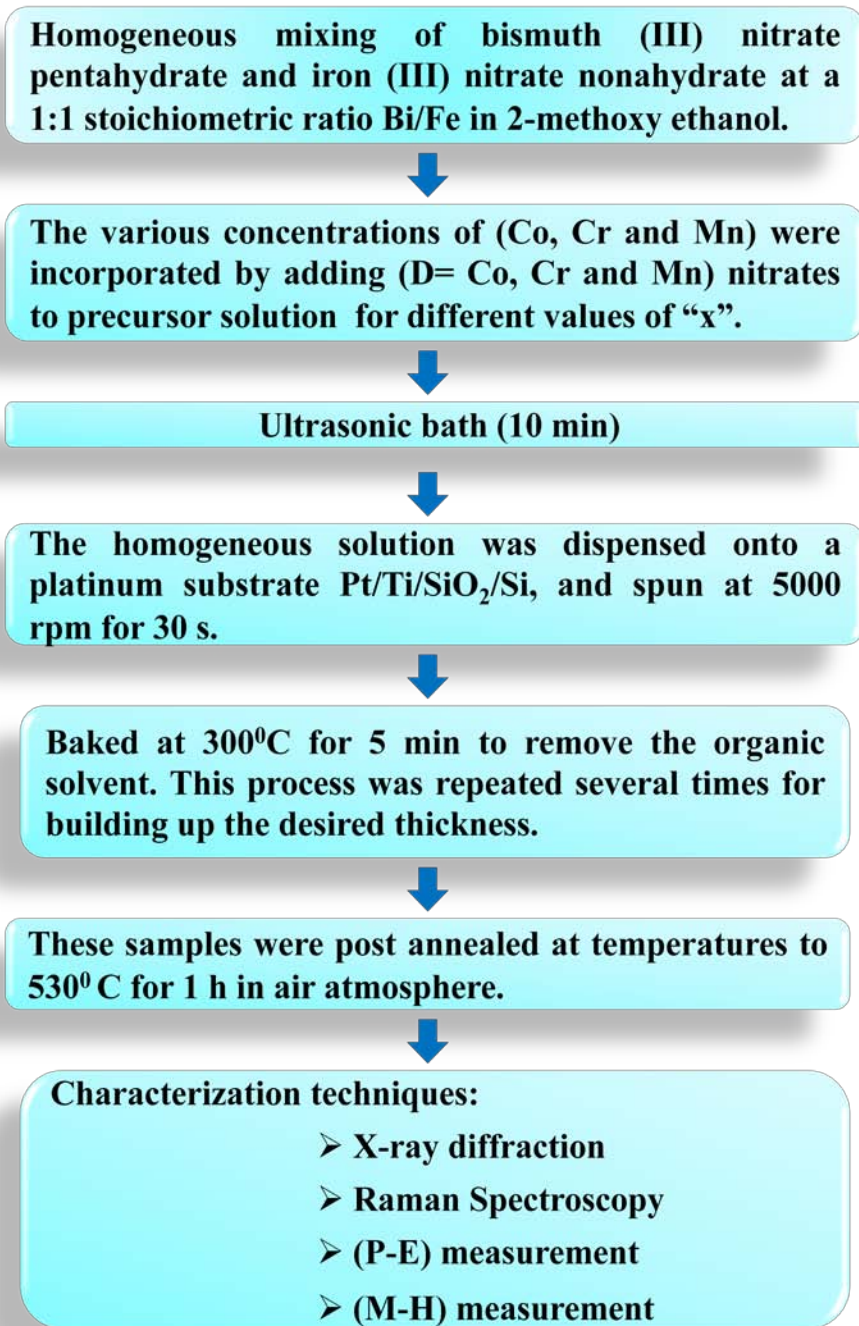
Figure 4.1 Flow diagram of the sol-gel spin coating of $BiFe_{1-x}D_xO_3$ (D= Co, Cr and Mn) thin films.

4.3 Characterization of the samples.

Structural analysis of the thin films was carried out in Siemens D5000 x-ray diffractometer (XRD) using the Cu Kα radiation (0.15405 nm). The vibrational spectra of the samples were analyzed by Raman spectroscopy using a 109 mW and 532 nm laser spectra physics, Renishaw nnova 300 coherent Raman microscope. The magnetic properties were characterized using a Lake Shore's new 7400 series Vibrating Sample Magnetometer (VSM). The ferroelectric hysteresis loops were measured with a RT 6000 HVS ferroelectric tester (Radiant technology). The thicknesses of the films were measured by the reflectance measurement method by a Filmetrics F-series. Electrical measurements were performed using a Pt-ferroelectric thin film-Pt capacitor configuration. These capacitors were fabricated by depositing Pt top electrodes on the surface of the thin film with an area of 4.9×10^{-4} cm^2 and utilizing the masking technique by dc sputtering. The FEI PTM 600 Scanning Electron Microscopy (SEM) technique was used for qualitative analyses of the average particle size and grain size, and identifies phase composition and microstructures defects.

4.3.1 X-ray Diffraction (XRD)

The X-ray diffraction (XRD) is a characterization technique used to analyze the structural properties of an object and substance. The XRD is a tool which is useful to determine the lattice parameters, the strain and the grain size; moreover it can identify the phases present in each sample. The X-ray is generating by irradiation of the Cu metal with high energy electrons. The electrons generate that the Cu atoms expel electrons out of their orbits but because of the tendency to keep the lowest energy state, electrons in the Cu atom fill the vacancies in lower levels, generating liberation of energy in form of X-ray. The X-ray beam passes through a slit with an established aperture to limit the wavelength of the beam, this X-ray inside the sample and strikes the atoms depending on the atomic structure and type of the atom. Once the beam strikes a plane of atoms with an angle θ with respect to the normal, the X-ray direction changes and a path length difference is proportional to sin θ arises for X-ray reflected by each plane. When the path length difference between reflections from adjacent planes is an integer multiple *n* of the wavelength λ, then constructive interference occurs and the angle between the diffracted beam and the transmitted beam is 2θ, and *d* is the interplanar spacing [47].

4.3.2 Raman Spectroscopy

Raman scattering is a powerful light scattering technique used to diagnose the internal structure of molecules and crystals [72]. In a light scattering experiment, light of a known frequency and polarization is scattered from a sample. The scattered light is then analyzed for frequency and polarization. Raman scattered light is frequency-shifted with respect to the excitation frequency, but the magnitude of the shift is independent of the excitation frequency. This "Raman shift" is, therefore, an intrinsic property of the sample. Because Raman scattered light changes in frequency, the rule of conservation of energy dictates that some energy is deposited in the sample. A definite Raman shift corresponds to excitation energy of the sample (such as the energy of a free vibration of a molecule). In general, only some excitations of a given sample are "Raman active," that is, only some may take part in the Raman scattering process. Hence the frequency spectrum of the Raman scattered light maps out part of the excitation spectrum.

4.3.3 Vibrating Sample Magnetometer (VSM)

VSM is an instrument based on the principle of electromagnetic induction. Its basic structure is schematically shown in Figure 4.2, which consists of a pick-up coils, and a field sensor. A maximum field de 30 kOe is obtained from an electromagnet field system. If a field higher than this is required, a superconducting magnetic can be used which is capable of producing a field as high as 160 kOe. The test sample (usually less than 10 mm square in size) in a uniform magnetic field can be treated as a magnetic dipole. The magnetic flux from the sample, which vibrates in the direction perpendicular to the applied field, induces an emf in the pick-up coil positioned nearby. This emf is proportional to the magnetic moment of the sample and is given by:

$$e = \frac{3}{4\pi}\mu_0 M w g_1 \tag{17}$$

Where M is the magnetic moment of the test sample, w is the angular velocity of the vibration, and g_1 is the instrument factor. The value of this is determined by measuring a sample with a known magnetic moment (calibration sample).

Figure 4.2 Vibrating Sample Magnetometer (VSM) [84].

After calibration with a standard sample, the output from the pick-up coil represents the value of the magnetic moment of the sample, and the output from the field sensor gives the applied field value. The output of the instrument is therefore an M-H loop or, more accurately, a curve showing the field dependence of the magnetic moment of the test sample, from which many magnetic parameters can be obtained. VSM is one of the most commonly used magnetometers for the characterization of magnetic materials in both the research laboratory and the production factory. The ultimate sensitivity of a modem VSM is as high as 10^{-6} emu. And the field resolution can be as small as 1 mOe. It is widely used for measurements of soft magnetic films (H_C and M_S).

4.3.4 Ferroelectric Tester

The polarization versus electric field (P-E) hysteresis loop of the capacitor was measured using the RT 6000 HVS ferroelectric tester (Radiant technology). The simplest method for measuring spontaneous polarization is the Sawyer and Tower method [68] as shown in Figure 4.3, in which C is the capacitance of the ferroelectric thin films and C_0 is the standard capacitor. The voltage across C should be sufficiently large to render a saturation in polarization, so V_0 should be proportional to the polarization charge, $V_0 = AP/C_0$, where A is the area of the

specimen. V is the applied voltage, which is usually an AC signal voltage of low frequencies. Thus, the applied field across the specimen is $E = V_C/d = (V-V_0)/d$. Where d is the thickness of thin films in centimeters
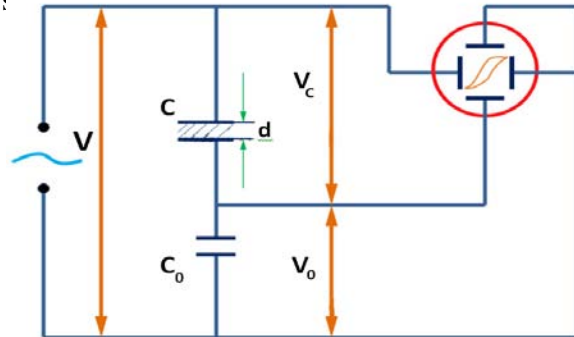

Figure 4.3 The Sawyer Tower method for the measurement of the polarization-electric field (P-E) characteristics [41].

4.3.5 Scanning Electron Microscopy (SEM)

Scanning electron microscopy gives the morphological and topographical information of the solid surfaces that is necessary in understanding the behavior of the surfaces [27]. In SEM, the sample is bombarded with an electron beam. The shorter wave length of electrons creates a better resolution than in optical microscopy. For the electrons to be able to pass through the sample, the sample should be conductive. In case of a non-conductive sample a layer of gold is sputtered on the surface of the sample. The electron beam, emitted from the filament in the electron gun, is accelerated towards the sample and focused by several condenser lenses. When the focused beam hits a point on the sample, numerous collisions between the electrons from the beam and atoms in the sample will occur. As a result of these collisions, some of the outer most electrons will be detached from the sample. These electrons, called secondary electrons, have relatively low kinetic energy and can easily be attracted by the detector. The detector counts the number of electrons emitted from this small area and the result is displayed as point on a computer screen. A magnified image of the sample is created by scanning the electron beam over a small area, detecting and displaying the number of electrons originating from each point. Both the topography of the sample and the atom numbers effect the number of secondary electrons emitted and these factors are therefore represented in the picture. The resulting image has shadows and perspective, much like ordinary photographs, and is consequently rather easy to interpret.

5. RESULTS AND DISCUSSION

5.1 X-ray diffraction studies

This thesis reports the structure, ferromagnetic and ferroelectric properties of the $BiFe_{1-x}D_xO_3$ films, where $D = Co$, Cr and Mn, deposited on $Pt/Ti/SiO_2/Si$ substrates by the previously described Sol-Gel process. X-ray diffraction patterns of the $BiFeO_3$ and $BiF_{1-x}Co_xO_3$ (BFCO) (x = 0.01, 0.02) films on Pt substrate ($Pt/Ti/SiO_2/Si$) are shown in Figure 5.1. The average films thicknesses were 0.5 µm, for all samples.

The observed diffraction peaks for BFCO suggests the formation of rhombohedral perovskite structure with the space group R3c [69], and no secondary phases related to cobalt oxide are detected, indicating the incorporation Co to Fe sites. In pure $BiFO_3$ (BFO), the (104) and (110) are observed, but the slight shift and overlap of these peaks is observed in $BiFe_{1-x}Co_xO_3$, which could be attributed to a small distortion in crystal structure due the lower ionic radii of Co^{2+} ion (0.082 nm) replacing Fe^{2+} ion (0.087 nm) [85].
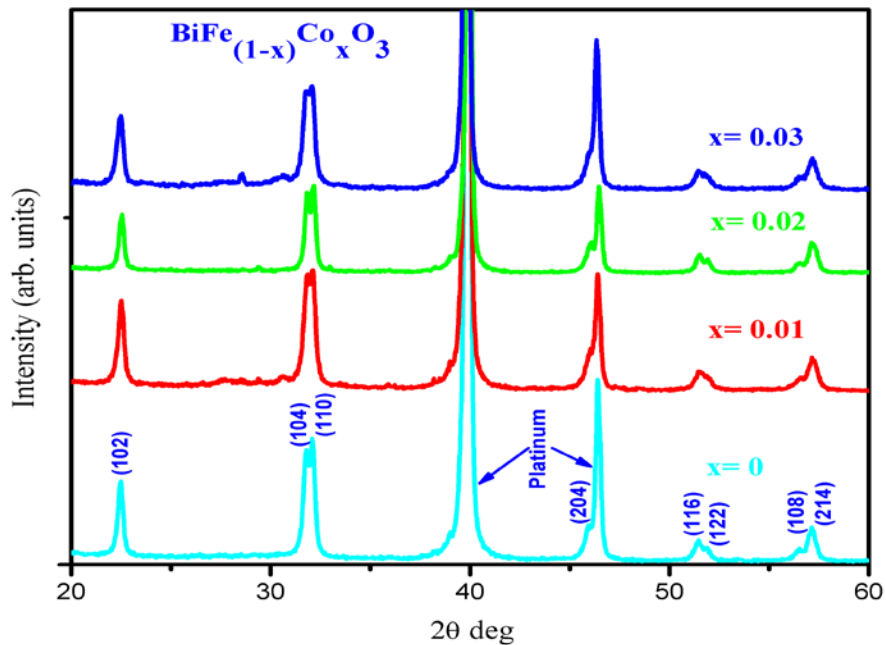

Figure 5.1 X-ray diffraction pattern for $BiFeO_3$ and $BiFe_{1-x}Co_xO_3$ thin films.

The Figure 5.2 shows XRD patterns of the $BiFeO_3$ and $BiF_{1-x}Mn_xO_3$ (x = 0.04, 0.07) films on $Pt/Ti/SiO_2/Si$ substrates. The observed diffraction peaks suggests the formation of rhombohedral perovskite structure with the space group R3c [69], and no secondary phases are detected. In pure BFO, the (104) and (110) peaks could be seen however with a slight shift, and the overlap of the peaks observed could be attributed to a small distortion in crystal structure due the higher ionic radii of Mn ion [86].
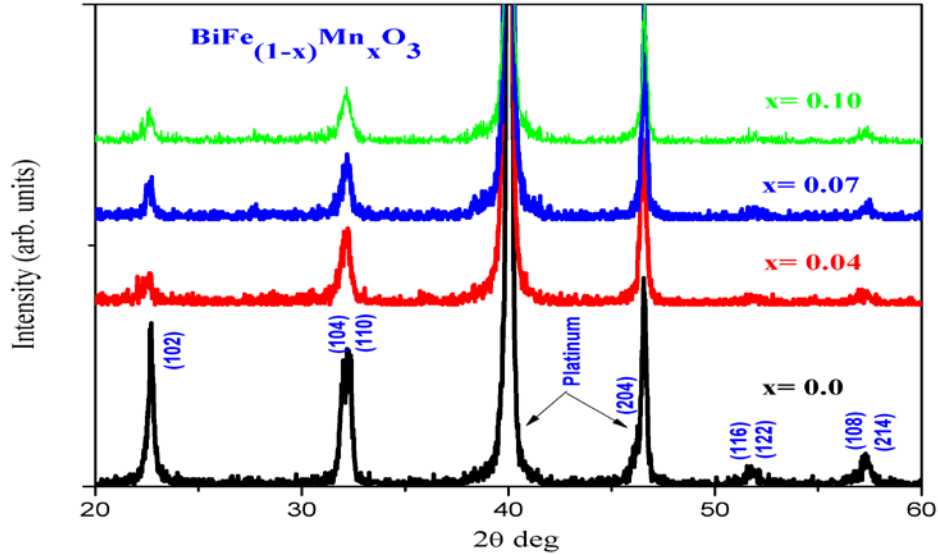

Figure 5.2 X-ray diffraction pattern for $BiFeO_3$ and $BiFe_{1-x}Mn_xO_3$ thin films.

X-ray diffraction patterns of $BiFeO_3$ and $BiFe_{1-x}Cr_xO_3$ (x = 0.02-0.04) films were studied on $Pt/Ti/SiO_2/Si$ structures. The XRD peaks are indexed using a rhombohedral structure. As shown in the Figure 5.3, all the films are composed of polycrystalline grains with a single perovskite phase. The preferred orientation along (110) axis and the broadening of some diffraction peaks are observable, as the Cr concentration is increased. It was observed that a single perovskite phase was formed up to a Cr concentration of 4%. Figure 5.3 displays a close up view of the 31 to 33 two-theta region comprising the (104) and (110) diffraction peaks of rhombohedral BFO. It is seen that there is a change in crystal structure with the increase of Cr concentration. Pure BFO and low 3% doping level of Cr exhibit distinct (104) and (110) peaks, however further addition of Cr up to 4% leads to the appearance of only a single peak in the spectral region corresponding to a loss of anisotropy and a change to a pseudocubic phase.

Further additions of Cr up to 5% also show only a diffraction peak in this range. The relative broadness of the 110 peak with 5% Cr addition is believed to be the result of the small grain size.
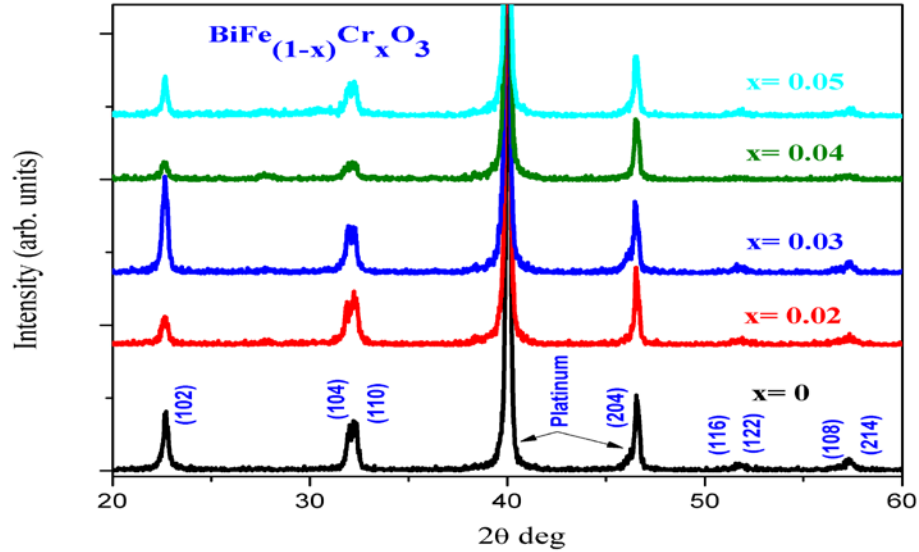

Figure 5.3 X-ray diffraction pattern for $BiFeO_3$ and $BiFe_{1-x}Cr_xO_3$ thin films.

5.2 Raman spectroscopic measurements

The Raman active modes of the rhombohedral BFO with R3c structure can be summarized using the irreducible representation $\Gamma = 4A_1 + 9E$ [70, 71]. Fukumura et al. [72] reported 13 Raman peaks at 4K predicted by group theory for single crystal BFO consisting four A_1 modes at 147, 176, 227, and 490 cm^{-1} and the remaining E modes at 77, 136, 265, 279, 351, 375, 437, 473 and 525 cm^{-1}. At room temperature, three most intense A_1 modes appear [71] at 138, 170, and 214 cm^{-1} in BFO films deposited by pulsed laser deposition (PLD).

In the present study, the room temperature Raman spectra of BFO and Co substituted BFO, deposited by spin coating, were taken in crossed polarization configurations and are shown in Figure 5.4. One can observed that the dominant A_1 modes (115, 148, 170, and 222 cm^{-1}) and several peaks assigned to E modes which are similar as in BFO single crystal and films deposited by PLD [71]. It is known that sample preparation methods influence the oxygen stoichiometry [71]. This is expected to show changes in oxygen bonding and disorder that is reflected in the vibrational frequencies of mode involving oxygen. The slight difference in some of the peak

43

positions observed can be attributed to the method of sample preparation. For comparison, Raman spectra of $BiCo_xFe_{1-x}O_3$ (x = 0.01 and 0.02) thin films prepared by sol-gel process as BFO, is also shown in Figure 5.4. We observe that A_1 mode at 115, 170, and 222 cm^{-1} maintains, while 148 cm^{-1} diminishes as Co content is increased. Because of the polycrystalline nature of the films, all A_1 modes cannot completely disappear in the crossed polarization configuration as observed in $BiCo_xFe_{1-x}O_3$ films.

Figure 5.4. Raman spectra of $BiFe_{1-x}Co_xO_3$ on platinum $Pt/Ti/SiO_2/Si$ substrate.

Raman spectra of $BiMn_xFe_{1-x}O_3$ (x = 0.04 and 0.07) thin films, prepared by sol-gel process as BFO, is also shown in Figure 5.5. We observe that A_1 mode at 115, 170, and 222 cm^{-1} maintains, while at 148 cm^{-1} diminishes as the Mn content is increased. For another hand, the mode 15 cm^{-1} disappeared for x= 0.07. Because of the polycrystalline nature of the films, all A_1 modes cannot completely disappear in the crossed polarization configuration as observed in $BiMn_xFe_{1-x}O_3$ films.

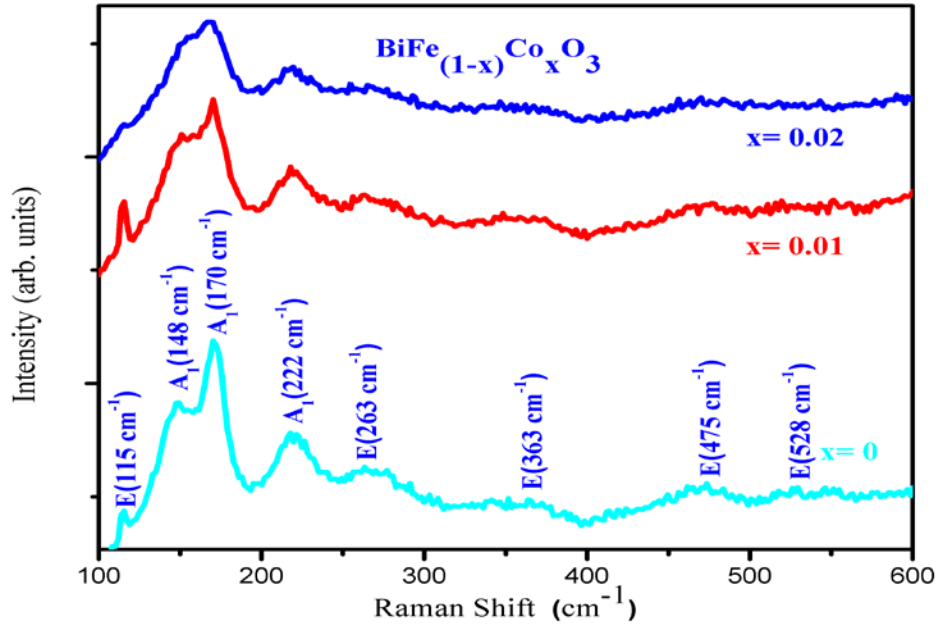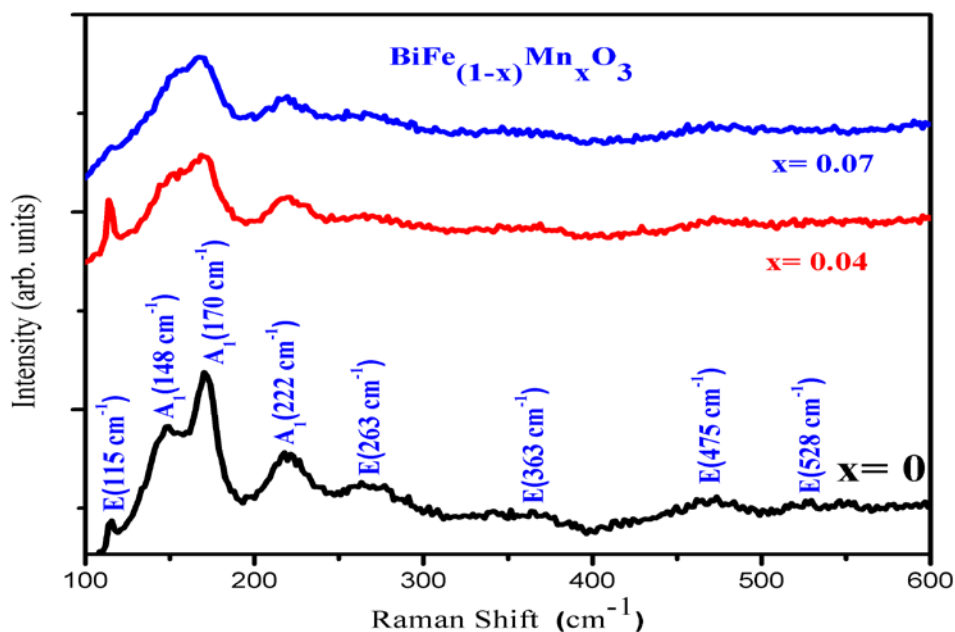**Figure 5.5** Raman spectra of $BiFe_{1-x}Mn_xO_3$ on platinum Pt/Ti/SiO$_2$/Si substrate.

The Raman peak 170 cm^{-1} shifts to higher frequency and broaden gradually with increasing concentration of Cr. This phenomenon is due to the induced bond shortening and lattice distortion. It is striking to find that the peak at around 115 cm^{-1} (denoted as *E* mode) disappears at 7% because the phase no maintains, indicating that the ion Cr is distorting the lattice. Such an anomaly may be correlated with a structural reordering in BiFeO$_3$, at least locally. The Raman spectroscopy data of the BiFeO$_3$ thin films crystallized at 525°C for 1 h on Pt/Ti/SiO$_2$/Si substrate are in good agreement with the X-ray diffraction pattern, showing that the films are rhombohedrally distorted perovskite BiFeO$_3$. Figure 5.6 displays the room temperature Raman spectra of thin film of BiFeO$_3$ on Pt/Ti/SiO$_2$/Si substrate. Our thin films show the presence of the R3c symmetry; the wide bands feature indicates a small crystalline size. We observe that the A$_1$ mode at 115, 170, and 222 cm^{-1} maintains, while 148 cm^{-1} diminishes as the content is increased.
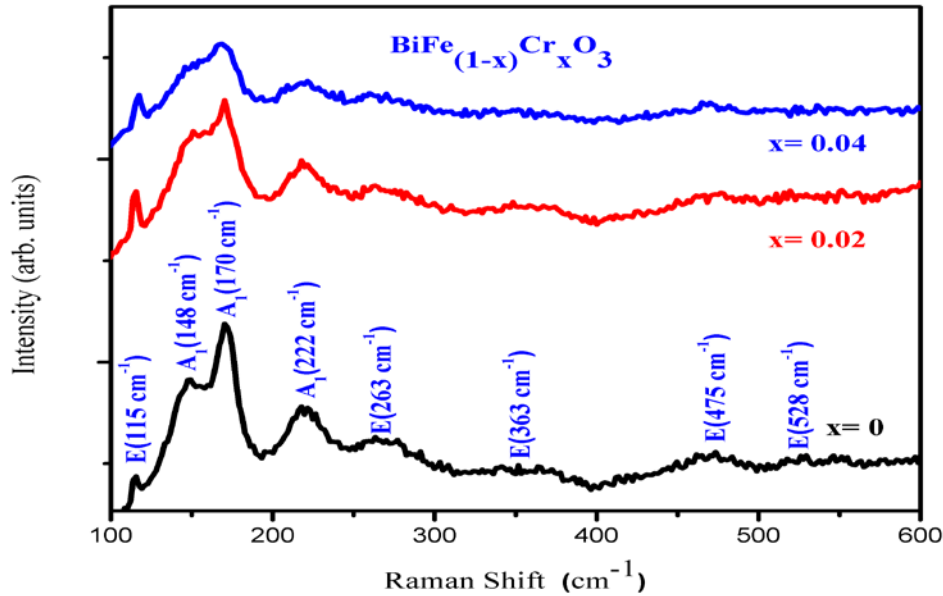
Figure 5.6 Raman spectra of $BiFe_{1-x}Cr_xO_3$ on platinum Pt/Ti/SiO$_2$/Si substrate.

5.3 Ferromagnetic measurements

The magnetic hysteresis (M-H) on $BiFeO_3$ and Co-doped $BiFeO_3$ thin films, measured by VSM at room temperature, are shown in Figure 5.7. Pure BFO film showed negligible hysteresis, but $BiFe_{1-x}Co_xO_3$ (x = 0.02) showed magnetization of ~3 emu/cm^3 and the coercive field H_C ~200 Oe. The increase in the macroscopic magnetization of Co substituted BFO may be attributed to the strained lattice [73] as observed in $BaTiO_3$-$CoFe_2O_4$ composite [66]. It is known that Fe^{2+} ions are responsible for macroscopic magnetization in BFO based materials [74]. Thus, the observed increase in magnetization for $BiFe_{1-x}Co_xO_3$ (x = 0.02) could be attributed to a favorable change in the exchange interaction leading to enhanced ferromagnetic properties along with increased stress in the crystal structure by partial replacement of Fe^{2+} ion by Co^{2+} ion.

Figure 5.8 shows the hysteresis curve (H-M) of the $BiFe_{1-x}Mn_xO_3$ samples at room temperature. The coercivity and saturation magnetization increases with increase in Mn concentration. The coercivity for $BiFe_{1-x}Mn_xO_3$ is 75 Oe and saturation magnetization is 2.5 emu/cm^3.
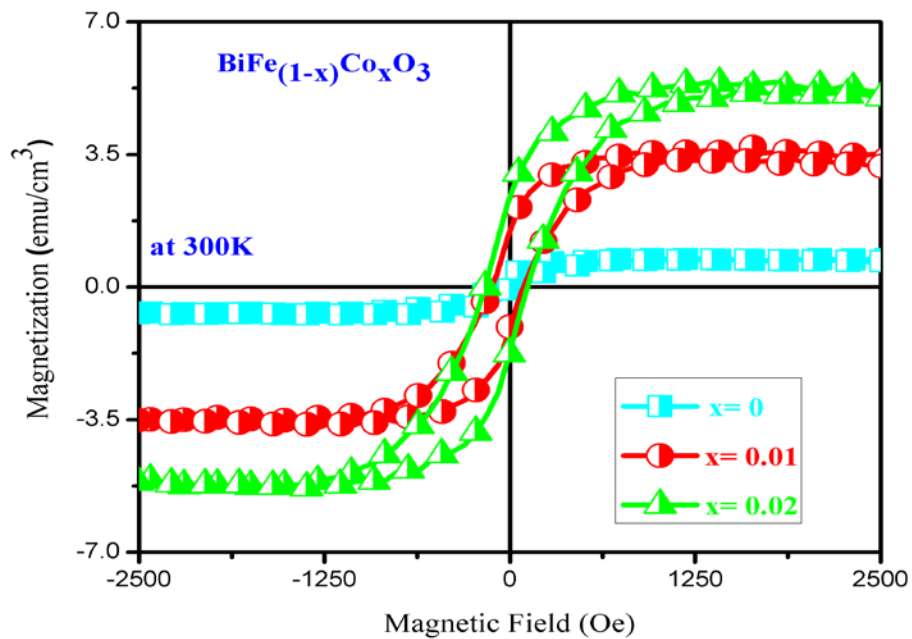
Figure 5.7 M-H curve of the $BiFeO_3$ and $BiFe_{1-x}Co_xO_3$ films at room temperature.
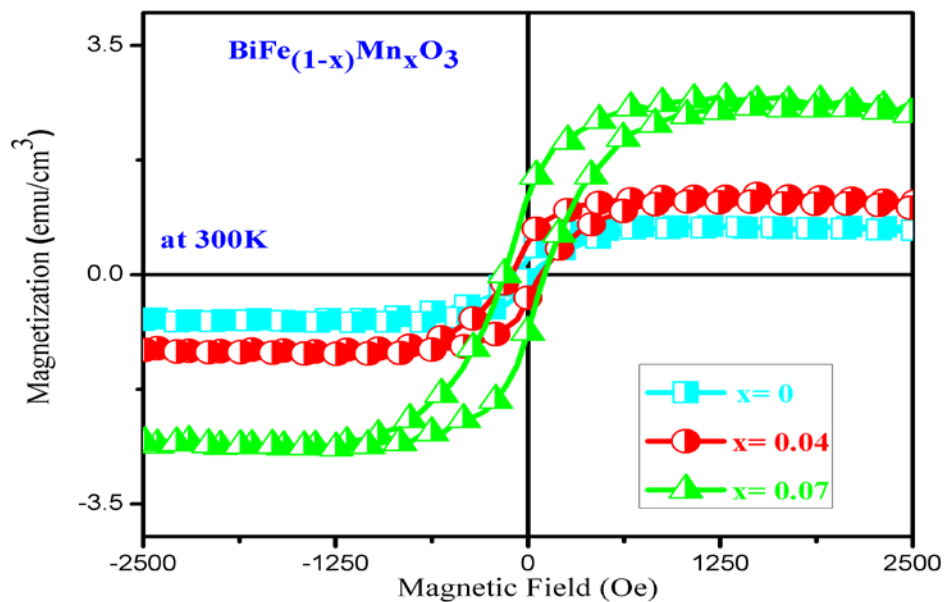

Figure 5.8 M-H curve of the $BiFeO_3$ and $BiFe_{1-x}Mn_xO_3$ films at room temperature.

Figure 5.9 shows the hysteresis curve (H-M) of the $BiFe_{1-x}Cr_xO_3$ samples at room temperature. The coercivity and saturation magnetization increases with increase in Cr concentration. The coercivity for $BiFe_{1-x}Cr_xO_3$ is 240 Oe and saturation magnetization is 10.8 emu/cm^3.
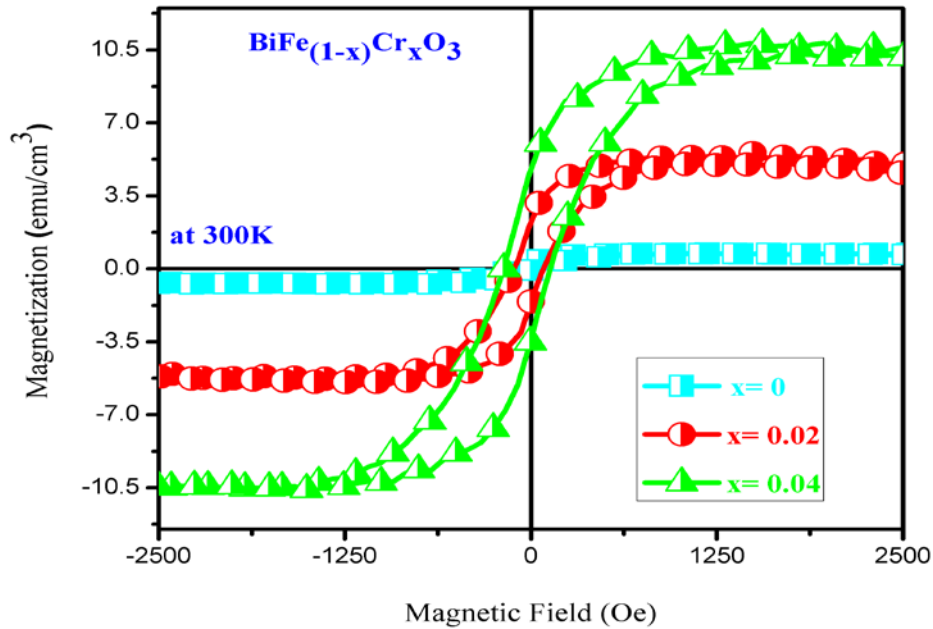
Figure 5.9 M-H curve of the $BiFeO_3$ and $BiFe_{1-x}Cr_xO_3$ films at room temperature.

Table 5.1 shows the values of remnant magnetization and coercive field for the maxima value of "x", when no exist changes in the phase.

Table 5.1 Values of remnant magnetization and coercive field when no changes the phase.

Thin films	x	M_r(emu/cm^3)	H_r(Oe)
$BiFe_{1-x}Co_xO_3$	0.02	3	140
$BiFe_{1-x}Mn_xO_3$	0.04	0.8	75
$BiFe_{1-x}Cr_xO_3$	0.04	5	160

5.4 Ferroelectric measurements

The ferroelectric response was tested using RT 6000 HVS probe. The top platinum (Pt) electrodes, of diameter 450 µm were deposited by RF sputtering. The measured ferroelectric response of $BiFeO_3$ and $BiFe_{1-x}Co_xO_3$ films (at 10 kHz and applied electric field 170 $kVcm^{-1}$) is shown in Figure 5.10. Although, saturation was not achieved, remnant polarizations (Pr) of 0.4 µC cm^{-2} for BFCO and very week 0.08 µC cm^{-2} for BFO were observed. According to Wang [15], the ferroelectricity of BFO originates from the displacements of Bi relative to the Fe-O octahedron along (111). In general, there are two types of ferroelectricity in BFO films prepared by different methods. In one type, Pr is few µC cm^{-2} and it is usually obtained at relatively low applied fields and the hysteresis loops are not saturated; while in the other type, high Pr values are obtained under high applied fields (usually several hundred kV cm^{-1}) and the hysteresis loops are well saturated [3].

Figure 5.10 P-E curves for $BiFeO_3$ and $BiFe_{1-x}Co_xO_3$ on platinum $Pt/Ti/SiO_2/Si$ substrates.

Figure 5.11 shows the ferroelectric response of the doped and undoped $BiFeO_3$ films at room temperature. The $BiFeO_3$ film shows a poor saturation polarization, Pr = 0.08 µC/cm^2. However, the $BiFe_{1-x}Mn_xO_3$ (x = 0.04) film revealed are improved ferroelectric polarization, Pr= 1 µC/cm^2, probably due to a reduction in the ionic conductivity of the film.
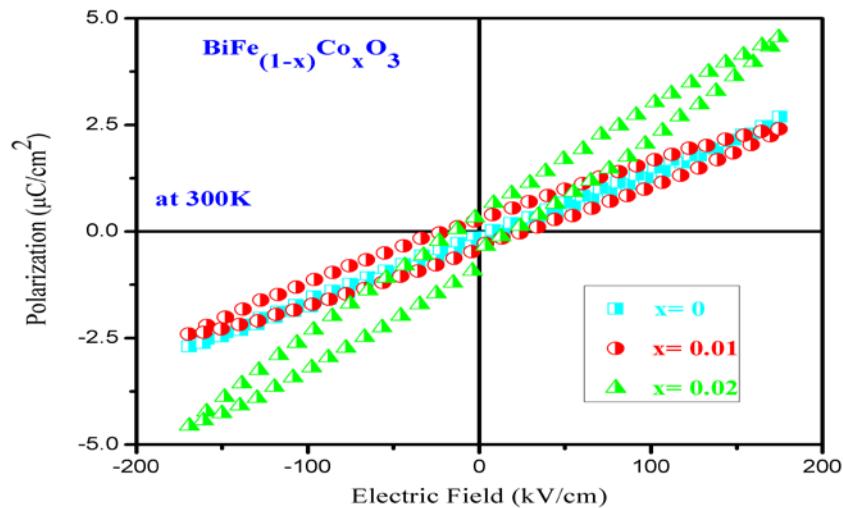
Figure 5.11 P-E curves for $BiFeO_3$ and $BiFe_{1-x}Mn_xO_3$ on platinum $Pt/Ti/SiO_2/Si$ substrates.

Figure 5.12 shows the ferroelectric response of the doped and undoped $BiFeO_3$ films at room temperature. $BiFeO_3$ film shows a poor saturation polarization, $Pr = 0.08$ $\mu C/cm^2$. However, $BiFe_{1-x}Cr_xO_3$ (x = 0.04) film revealed the improved ferroelectric polarization, $Pr = 2$ $\mu C/cm^2$, probably due to a reduction in ionic conductivity of the film.

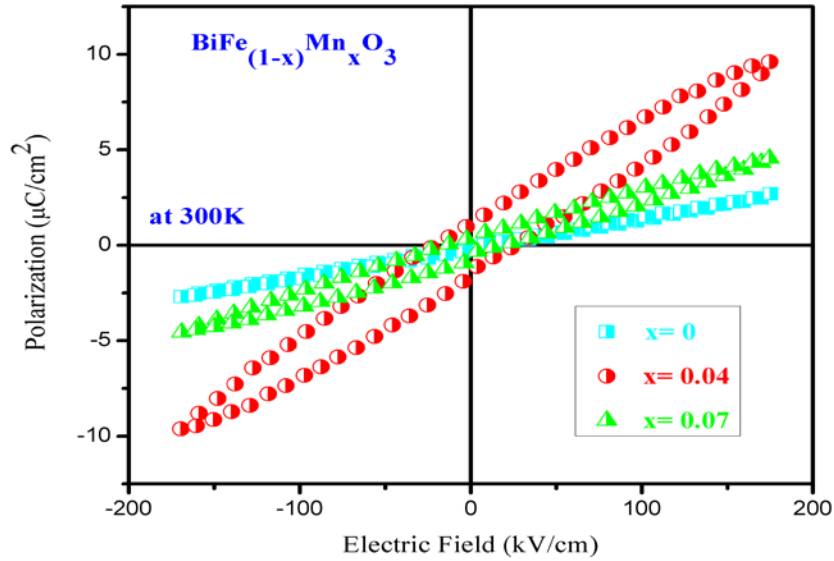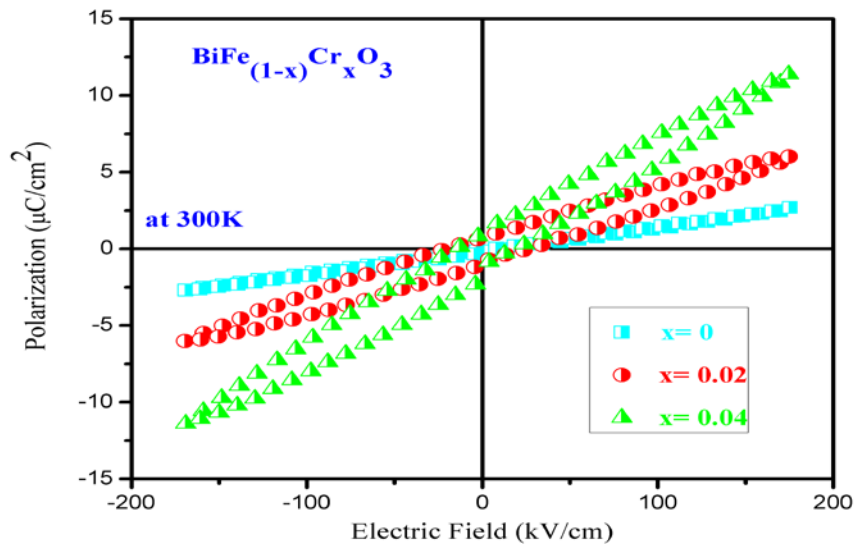**Figure 5.12** P-E curves for $BiFeO_3$ and $BiFe_{1-x}Cr_xO_3$ on platinum $Pt/Ti/SiO_2/Si$ substrates.

50

Table 5.2 shows the values of remnant polarization and coercive field for the maxima value of "x", when no exist changes in the phase.

Table 5.2 Values of remnant polarization and coercive field when no changes the phase.

Thin films	x	$P_r (\mu C\ cm^{-2})$	$E_r (kV/cm)$
$BiFe_{1-x}Co_xO_3$	0.02	0.4	18
$BiFe_{1-x}Mn_xO_3$	0.04	1	23
$BiFe_{1-x}Cr_xO_3$	0.04	2	19

5.5 SEM studies

SEM studies evidenced the morphology of the thin film. Figure 5.13 shows surface micrographs of the $BiFeO_3$. Figure 5.13(a) is taken from the reference [75] and the Figure 5.13(b) we shows the surface of $BiFeO_3$ films on Pt/Ti/SiO$_2$/Si substrate after annealing at 530^0C for 60 min in air atmosphere. SEM picture reveal that the matrix is uniform and no segregation of impurity phase is detected.

Figure 5.13   SEM images of (a) Images taken from the reference [75], and (b) surface of $BiFeO_3$ films on Pt/Ti/SiO$_2$/Si substrate (prepared at the laboratory).

6. STUDIES ON COMPOSITE MULTILAYER

6.1 Crystal structure $Bi_4Ti_3O_{12}$

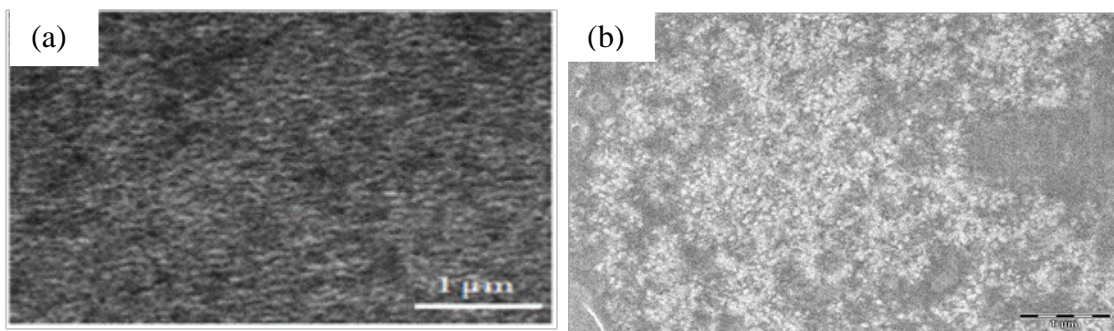The Curie temperature of $Bi_4Ti_3O_{12}$ is 675^0C [76], which make it a suitable candidate for high-temperature piezoelectric devices. $Bi_4Ti_3O_{12}$ belongs to the family of the Aurivillius compounds [77]. The crystal structure of $Bi_4Ti_3O_{12}$ consists of $(Bi_2O_2)^{2+}$ sheets alternating with $(Bi_2Ti_3O_{10})^{2-}$ layers along the pseudotetragonal c-axis, as shown in Figure 6.1 [76]. In the $Bi_2Ti_3O_{10}$ units, Ti ions are enclosed by oxygen octahedra, which are linked through corners forming the O-Ti-O linear chains. The Bi ions occupy the spaces in the framework of TiO_6 octahedra. The $Bi_2Ti_3O_{10}$ units exhibit a remarkable similarity to the perovskite structure. As established by Aurivillius [77], $Bi_4Ti_3O_{12}$ has orthorhombic symmetry with room temperature lattice parameters are a=5.410, b=5.448, and c=32.84 Å. $Bi_4Ti_3O_{12}$ exhibits highly anisotropic properties due to the layered structure, with maximum electrical conductivity in the same plane as polarization [78]. It is interesting that $Bi_4Ti_3O_{12}$ shows relatively worse fatigue properties [79]. Although it has the layered perovskite structure with $(Bi_2O_2)^{2+}$ layers, the origin of the fatigue behavior of $Bi_4Ti_3O_{12}$ thin films was studied by Park et al. [80]. They concluded that oxygen ions near the Bi ions are few stables due to the volatility of Bi. In $Bi_4Ti_3O_{12}$, oxygen vacancies can be induced both in the $(Bi_2O_2)^{2+}$ layers and in the TiO_6 octahedra layers. Thus, it was deduced that in the stability of the metal-oxygen octahedra is responsible for fatigue behaviors $Bi_4Ti_3O_{12}$. Therefore, the fatigue characteristics of $Bi_4Ti_3O_{12}$ could be improved by substituting of Bi ions near the Ti-O octahedra with other elements which make the oxygen ions stable. Doping of $Bi_4Ti_3O_{12}$ with Nd, substituting into the Bi site, yields the materials named bismuth neodymium titanate ($Bi_{4-x}Nd_xTi_3O_{12}$) (BNT) [81]. This doping allows one to improve fatigue characteristics, increase the remnant polarization, and decrease the process temperature of the material, albeit at the expense of an increased coercive field [80]. Piezoelectric properties of $Bi_4Ti_3O_{12}$ in co-relation to their structural and microstructural features are well described in a review [82].
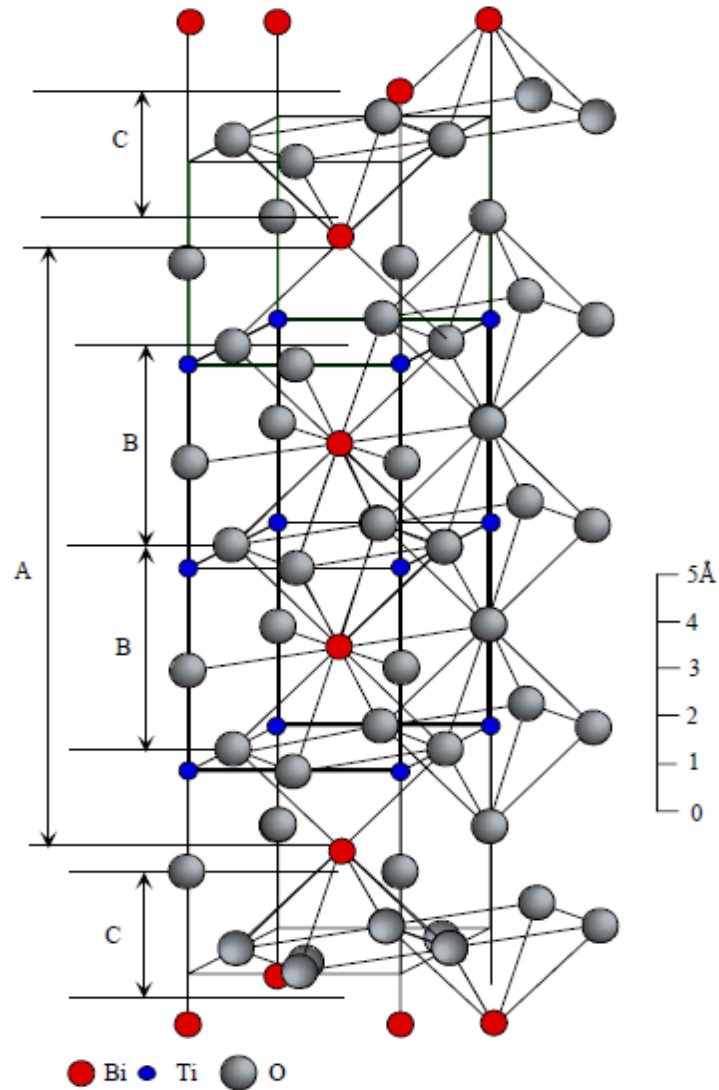
Figure 6.1 One half of the pseudotetragonal unit cell of $Bi_4Ti_3O_{12}$. A denotes the perovskite layer $(Bi_2Ti_3O_{10})^{2-}$; C denotes $(Bi_2O_2)^{2+}$ layers; and B, denotes a unit cell of hypothetical perovskite structure $BiTiO_3$ [76].

6.2 Crystal structure $CoFe_2O_4$

$CoFe_2O_4$ (CFO) has an inverse spinel crystal structure. The normal crystal structure of an AB_2O_4 spinel consists of the A^{2+} atoms occupying all of the tetrahedral coordination sites and the B^{3+} atoms occupying all of the octahedral sites [83]. In the case of an inverse spinel such as

$CoFe_2O_4$, the Co cation occupies one half of the octahedral coordination sites. Half of the Fe^{3+} cations occupie the other half of the octahedral coordination sites as well as all of the tetrahedral coordination sites. The crystal structure of $CoFe_2O_4$ is shown in Figure 6.2.
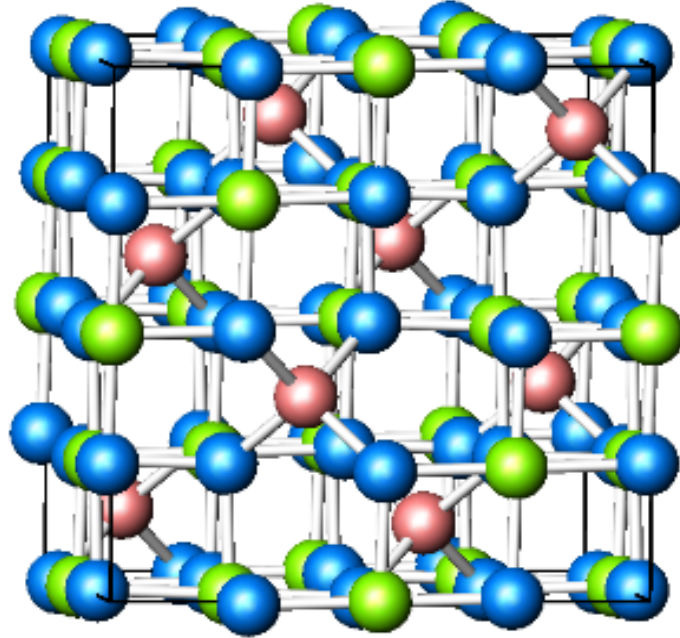
Figure 6.2 Crystal structures of $CoFe_2O_4$, where green spheres are Co, pink spheres are Fe, and blue spheres are O.

6.3 Horizontal multilayer

Great strides have been made in the area of composite magnetoelectric systems. These systems operate by coupling the magnetic and electric properties between two materials, generally a ferroelectric material and a ferrimagnetic material, via strain. An applied electric field creates a piezoelectric strain in the ferroelectric, which produces a corresponding strain in the ferrimagnetic material and a subsequent piezomagnetic change in magnetization or the magnetic anisotropy [52]. $Bi_{4-x}Nd_xTi_3O_{12}$ is an excellent ferroelectric material [81] and $CoFe_2O_4$ [83] is well known as ferrite. They can be grown in a single phase at about the same temperature (600^0C-700^0C). Therefore, their composite are attractive as multiferroics. Figure 6.3 shows the $Bi_{3.5}Nd_{0.5}Ti_3O_{12}$/$CoFe_2O_4$ alternate thin films fabricated on Pt/Ti/SiO$_2$/Si substrates by a simple spin coating technique (as describe elsewhere).
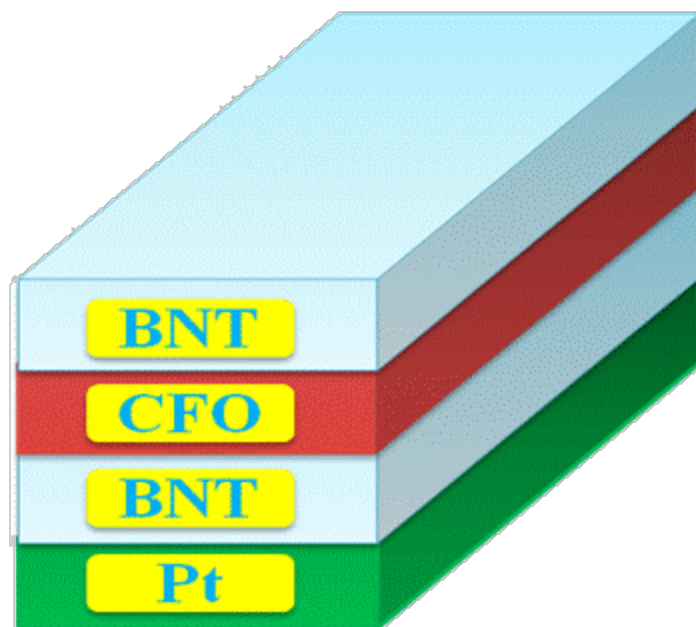
Figure 6.3 The composites films were fabricated on $Pt/Ti/SiO_2/Si$ substrates by a simple spin coating technique using alternate layers of $Bi_{3.5}Nd_{0.5}Ti_3O_{12}$ and $CoFe_2O_4$.

6.4 X-ray diffraction studies

We investigated the crystal structure of our composites using X-ray diffraction. Two sets of alternating layers were prepared. In the first case, 1-layer of each was alternated ten times, and in the second case, 3-layers of $Bi_{3.5}Nd_{0.5}Ti_3O_{12}$ were alternated by 1-layer of $CoFe_2O_4$ five times, on Pt substrate. After the post-annealing steps, X-ray diffraction of the composite film was recorded. For a clear comparison, Figure 6.4 shows the X-ray diffraction patterns of pure $CoFe_2O_4$ and $Bi_{3.5}Nd_{0.5}Ti_3O_{12}$, along with the two sets of composite films. No other phases were observed, but bismuth-layered perovskite $Bi_{3.5}Nd_{0.5}Ti_3O_{12}$ and spinel $CoFe_2O_4$ phases were observed in the composite films. Therefore, a composite film is formed, as revealed by the XRD patterns.
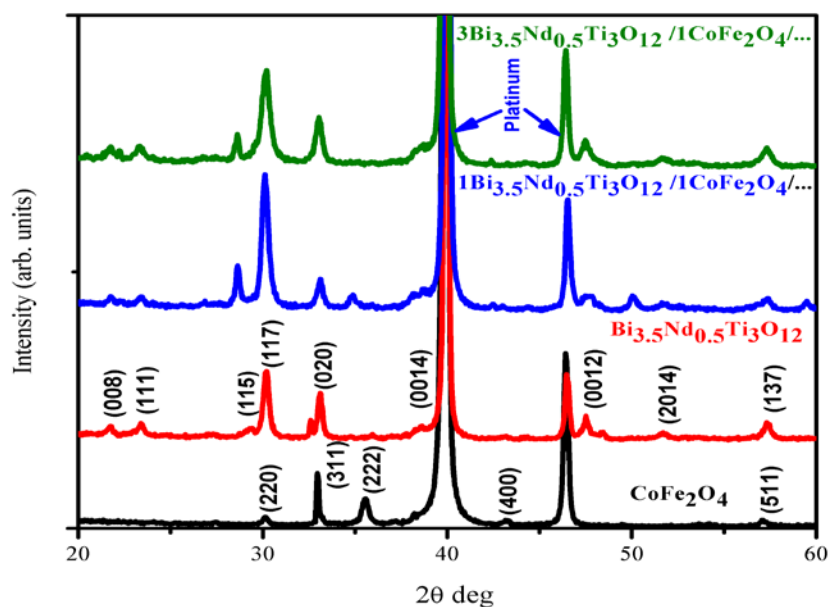
Figure 6.4 X-ray diffraction patterns for pure $CoFeO_4$ and $Bi_{3.5}Nd_{0.5}Ti_3O_{12}$ films. The XRD of a composite film made of 1-$Bi_{3.5}Nd_{0.5}Ti_3O_{12}$/1-$CoFe_2O_4$ (alternate one layer, case one), and also with 3-$Bi_{3.5}Nd_{0.5}Ti_3O_{12}$/1-$CoFe_2O_4$ (alternate three layers, case two) are shown.

6.5 Ferromagnetic measurements

Figure 6.5 shows the magnetic hysterisis (M-H) of the composites of case one and case two: 1-$Bi_{3.5}Nd_{0.5}Ti_3O_{12}$/1-$CoFe_2O_4$/….. and 3-$Bi_{3.5}Nd_{0.5}Ti_3O_{12}$/1-$CoFe_2O_4$/….., respectively. The magnitudes of the remnant magnetization M and the coercive field H_c for composite films (case one and case two) are measured to be 60 emu cm^{-3} and 1.49 kOe and 20 emu cm^{-3} and 0.7 kOe, respectively. From the hysterisis curves (M-H), one can observe that the magnetization M decreased when the number of $Bi_{3.5}Nd_{0.5}Ti_3O_{12}$ layers in the composite increased. This is expected because the possible magnetic coupling is depressed by the smaller amount of $CoFe_2O_4$.
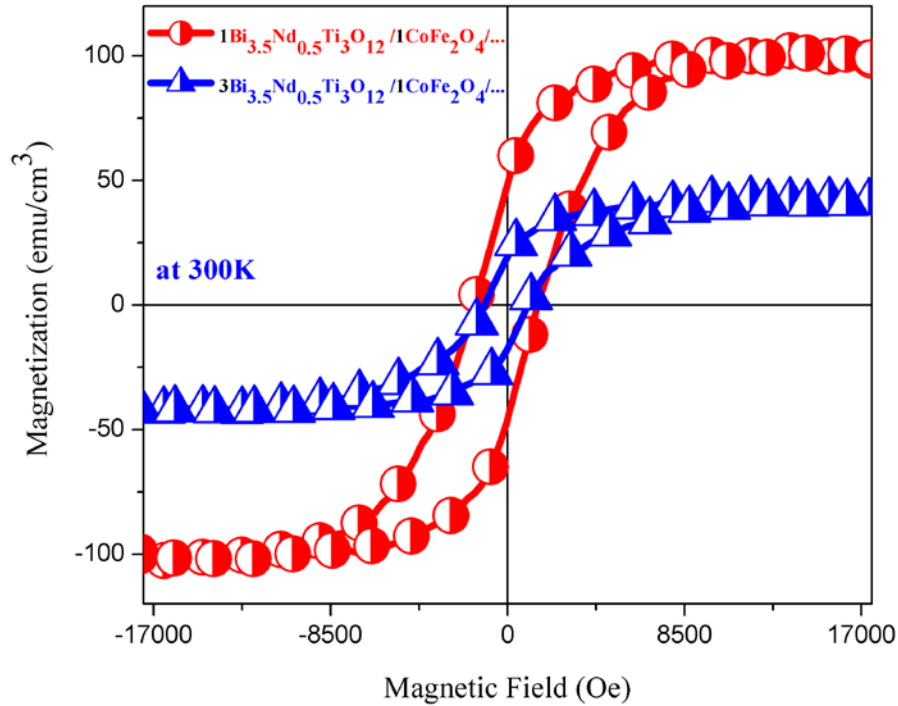
Figure 6.5 Ferromagnetic hysteresis loop for composite films (multilayer structures) at room temperature.

6.6 Ferroelectric measurements

The degradation of the electrical polarization of the composite film is expected due to the presence of non-ferroelectric $CoFe_2O_4$ region. Figure 6.6 shows the (P-E) curves of the $1\text{-}Bi_{3.5}Nd_{0.5}Ti_3O_{12}/1\text{-}CoFe_2O_4/\ldots$ and $3\text{-}Bi_{3.5}Nd_{0.5}Ti_3O_{12}/1\text{-}CoFe_2O_4/\ldots$ multilayers thin films. The magnitudes of the remnant polarization P_r and the coercive field E_c for $1\text{-}Bi_{3.5}Nd_{0.5}Ti_3O_{12}/1\text{-}CoFe_2O_4/\ldots$ and $3\text{-}Bi_{3.5}Nd_{0.5}Ti_3O_{12}/1\text{-}CoFe_2O_4/\ldots$ multilayers thin films are measured to be $1.5 \, \mu C/cm^2$ and $38 \, kV/cm$, and $2.82 \, \mu C/cm^2$ and $38 \, kV/cm$, respectively. The P_r value increased when the number of layer increased. Although in these initial results the saturation is not achieved, a remnant polarization is clearly observed in Figure 6.6. It will need some extensive research, but great possibilities exist in these multiferroic composites for practical multifunctional devices.
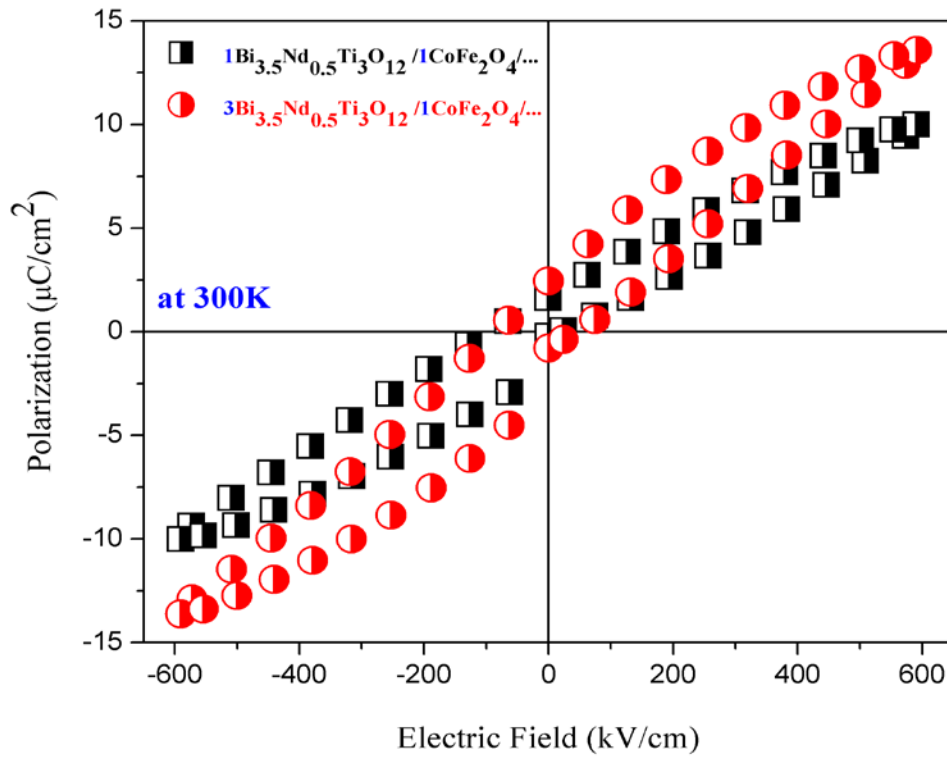
Figure 6.6 Ferroelectric hysteresis loop for composite films (multilayer structures) at room temperature.

Table 5.3 shows the values of remnant magnetization, magnetic coercive field, remnant polarization, and electric coercive field for different composites of case one and case two: 1-$Bi_{3.5}Nd_{0.5}Ti_3O_{12}$/1-$CoFe_2O_4$/….. and 3-$Bi_{3.5}Nd_{0.5}Ti_3O_{12}$/1-$CoFe_2O_4$/….., respectively.

Table 5.3 Values of remnant magnetization, magnetic coercive field, remnant polarization, and electric coercive field for different composites.

Thin films	M_r (emu/cm^3)	H_r (Oe)	P_r (µC cm^{-2})	E_r (kV/cm)
1 BNT/1 CFO/….	55	1575	1.5	60
3 BNT/1 CFO/….	21	860	2.8	80

7. CONCLUSIONS

In this thesis we have been successful in synthesizing a new system by a simple spin coating technique which exhibit multiferroic properties. The results of magnetic and electric measurements show coexistence of ferroelectric and ferromagnetic phenomena, opening the posibility of magnetoelectric coupling at room temperature. The material characteristic (magnetoelectric coupling at room temperature) may be highly useful in numerous devices. These materials are promising candidates for applications in memories, spintronics and magnetoelectric sensor devices.

We observed that a highly pure single phase $BiFeO_3$ can be grown by sol-gel spin-coating method. Their high resistivity allows observing a clear hysteretic polarization loop at room temperature, which confirms the ferroelectricity of $BiFeO_3$. We conclude that large polarizations are intrinsic to this material and do not stem from some particular property of the thin films. Our magnetic measurements reveal that $BiFeO_3$ has a pure antiferromagnetic response.

BFO, Cr-doped thin films were fabricated on $Pt/Ti/SiO_2/Si$ substrates by sol–gel spin-coating method. The XRD analysis revealed that all the films have the rhombohedral perovskite structure with the space group $R3c$. Excellent ferroelectric properties are obtained in the $BiFe_{1-x}Cr_xO_3$ film. Moreover, an enhanced ferromagnetism with Ms ~10.5 emu cm^{-3} is observed in this film. It is demonstrated that both the ferroelectric and ferromagnetic properties of the BFO film can be significantly enhanced by the Cr-doping. A very large remanent electrical polarization value of 1.5 $\mu C/cm^2$ was observed in $BiFe_{0.96}Cr_{0.04}O_3$ thin film on $Pt/Ti/SiO_2/Si$ substrate. As well as the ferroelectric performance improvement from Cr-doping, the Cr-doping also enhances the magnetic moment. It is expected that the solution to the problem of control of electrical leakage, which has been a severe obstacle restricting practical application, will give initial for a real devices based on $BiFeO_3$ thin films.

Co substitution has rhombohedral perovskite structure with the space group $R3c$ of $BiFeO_3$ up to x= 0.02. The magnetization has increased with an increase in Co concentration from x= 0.01 to x= 0.02. Ferroelectric and magnetic loops have been observed in the

$BiFe_{1-x}Co_xO_3$ thin films at room temperature, indicating that ferroelectric and magnetic orders coexist at room temperature. The ferromagnetic and ferroelectric orders coexist at room temperature, for a particular concentration i.e. $x = 0.04$ of Mn ion in $BiFe_{1-x}Mn_xO_3$. Comparing with my results, we observed that an increase in electric polarization and magnetization maintains the structure of BFO when is doped with chromium.

The composites films were grown as multilayers and showed that weak ferroelectric and ferromagnetic orders coexist at room temperature. The increased layers of (BNT) enhanced the ferroelectric response, but the ferromagnetic response decreased.

7.1. Suggestions for future works

We have demonstrated, for the first time, the magnetic and electric polarization in magnetic ion doped BFO and related materials at room temperature. Thus, they are potentially candidates for extensive research for magnetoelectric random – access memory devices.
The future work is required:

1) To optimize the film thickness and its effect on magnetoelectric coupling parameters.
2) New multi-layered composited such as $BaTiO_3$-$CoFe_2O_4$ structures using solution route.
3) New $YMnO_3$ & $FeMnO_3$ systems.

REFERENCES

[1] C. Michel, J. Moreau, G. Achenbach, R. Gerson, and W. James, The atomic structure of $BiFeO_3$, Solid State Commun., **7**, 701 (1969).

[2] Kubel, F., and Schmid, H., Structure of a ferroelectric and ferroelastic monodomain crystal of the perovskite $BiFeO_3$, Acta Crystallogr., Sect. B: Struct. Sci., **B46**, 698 (1990).

[3] Neaton, J. B., Ederer, C., Waghmare, U. V., Spaldin, N. A., and Rabe, K. M., First principles study of spontaneous polarization in multiferroic $BiFeO_3$, Phys. Rev. B., **71**, 014113 (2005).

[4] I. Sosnowska, W. Schäfer, W. Kockelmann, K. H. Andersen, and I. O. Troyanchuk, Crystal structure and spiral magnetic ordering of $BiFeO_3$ doped with manganese, Appl. Phys. A: Mater. Sci. Process., **74**, S1040 (2002).

[5] Sosnowska I., Peterlinneumaier T., and Steichele E., Spiral magnetic ordering in bismuth ferrite, J. Phys. C-Solid State Phys., **15**, 4835 (1982).

[6] Y. P. Wang, L. Zhou, M. F. Zhang, X. Y. Chen, J. M. Liu, and Z. G. Liu, Room temperature saturated ferroelectric polarization in $BiFeO_3$ ceramics synthesized by rapid liquid phase sintering, Appl. Phys. Lett., **84**, 1731 (2004).

[7] V. R. Palkar and R. Pinto, $BiFeO_3$ thin films: Novel effects, Pramana, J. Phys. **58**, 1003 (2002).

[8] V. R. Palkar, J. John, and R. Pinto, Observation of saturated polarization and dielectric anomaly in magnetoelectric $BiFeO_3$ thin films, Appl. Phys. Lett., **80**, 1628 (2002).

[9] W. M. Zhu and Z. G. Ye, Effects of chemical modification on the electrical properties of 0.67 BiFeO3-0.33 PbTiO3 ferroelectric ceramics, Ceram. International, **30**, 1435 (2004).

[10] M. Mahesh Kumar, S. Srinath, G. S. Kumar, and S. V. Suryanarayana, Spontaneous magnetic moment in $BiFeO_3$-$BaTiO_3$ solid solutions at low temperatures, J. Mag. Mag. Mat., **188**, 203 (1998).

[11] J. S. Kim, C. I. Cheon, C. H. Lee, and P. W. Jang, Weak ferromagnetism in the ferroelectric $BiFeO_3$-$ReFeO_3$-$BaTiO_3$ solid solutions (Re=Dy, La), J. Appl. Phys., **96**, 468 (2004).

[12] N. Wang, J. Cheng, A. Pyatakov, A. K. Zvezdin, J. F. Li, L. E. Cross, and D. Viehland, Multiferroic properties of modified $BiFeO_3$-$PbTiO_3$-based ceramics: Random-field induced release of latent magnetization and polarization, Phys. Rev. B, **72**, 104434 (2005).

[13] H. Paik, H. Hwang, N. Kwangsoo, S. Kwon, and D. Cann, Room temperature multiferroic properties of single-phase $(Bi_{0.9}La_{0.1})FeO_3$-$Ba(Fe_{0.5}Nb_{0.5})O_3$ solid solution ceramics, Appl. Phys. Lett., **90**, 042908 (2007).

[14] B. Ruette, S. Zvyagin, A. P. Pyatakov, A. A. Bush, J. F. Li, V. I. Belotelov, A. K. Zvezdin, and D. Viehland, Magnetic-field-induced phase transition in $BiFeO_3$ observed by high-field electron spin resonance: Cycloidal to homogeneous spin order, Phys. Rev. B, **69**, 064114 (2004).

[15] J. Wang, J. B. Neaton, H. Zheng, V. Nagarajan, S. B. Ogale, B. Liu, D. Viehland, V. Vaithyanathan, D. G. Schlom, U. V. Waghmare, N. A. Spaldin, K. M. Rabe, M. Wuttig, and R. Ramesh, Epitaxial $BiFeO_3$ Multiferroic Thin Film Heterostructures, Science, **299**, 1719 (2003).

[16] F. Bai, J. Wang, M. Wuttig, J. Li, N. Wang, A. P. Pyatakov, A. K. Zvezdin, L. E. Cross, and D. Viehland, Destruction of spin cycloid in (111) c-oriented BiFeO3 thin films by epitaxial constraint: enhanced polarization and release of latent magnetization, Appl. Phys. Lett, **86**, 032511 (2005).

[17] J. Teague, R. Gerson, and W. James, Dielectric hysteresis in single crystal $BiFeO_3$, Solid State Commun., **8**, 1073 (1970).

[18] K. Y. Yun, M. Noda, and M. Okuyama, Prominent ferroelectricity of $BiFeO_3$ thin films prepared by pulsed-laser deposition, Appl. Phys. Lett., **83**, 3981 (2003).

[19] K. Y. Yun, D. Ricinschi, T. Kanashima, M. Noda, and M. Okuyama, Giant ferroelectric polarization beyond 150 mu C/cm(2) in $BiFeO_3$ thin film, Jpn. J. Appl. Phys., Part 2, **43**, L647 (2004).

[20] K. Y. Yun, M. Noda, M. Okuyama, H. Saeki, H. Tabata, and K. Saito, Structural and multiferroic properties of $BiFeO_3$ thin films at room Temperature, J. Appl. Phys., **96**, 3399 (2004).

[21] K. Y. Yun, D. Ricinschi, T. Kanashima, and M. Okuyama, Enhancement of electrical properties in polycrystalline $BiFeO_3$ thin films, Appl. Phys. Lett., **89**, 192902 (2006).

[22] D. Ricinschi, K. Yun , M. Okuyama, First-principles study of $BiFeO_3$ films with giant polarization and its dependence on structural parameters, Ferroelectrics, **335**, 181 (2006).

[23] J. Li, J. Wang, M. Wuttig, R. Ramesh, N. Wang, B. Ruette, A. P. Pyatakov, A. K. Zvezdin, and D. Viehland, Dramatically enhanced polarization in 001, 101 and 111 $BiFeO_3$ thin films due to epitiaxial-induced transitions, Appl. Phys. Lett., **84**, 5261 (2004).

[24] W. Eerenstein, F. D. Morrison, J. Dho, M. G. Blamire, J. F. Scott, and N. D. Mathur Epitaxial $BiFeO_3$ Multiferroic Thin Film Heterostructures, Science, **307**, 1203a (2005).

[25] J. Wang, A. Scholl, H. Zheng, S. B. Ogale, D. Viehland, D. G. Schlom, N. A. Spaldin, K. M. Rabe, M. Wuttig, L. Mohaddes, J. Neaton, U. Waghmare, T. Zhao, and R. Ramesh, Epitaxial $BiFeO_3$ Multiferroic Thin Film Heterostructures, Science, **307**, 1203b (2005).

[26] S. Y. Yang, F. Zavaliche, L. M. Ardabili, V. Vaithyanathan, D. G. Schlom, Y. J. Lee, Y. H. Chu, M. P. Cruz, Q. Zhan, T. Zhao, and R. Ramesh, Metalorganic chemical vapor deposition of lead-free ferroelectric $BiFeO_3$ films for memory applications, Appl. Phys. Lett, **87**, 102903 (2005).

[27] R. Ueno, S. Okaura, H. Funakubo, and K. Saito, Crystal Structure and Electrical Properties of Epitaxial $BiFeO_3$ Thin Films Grown by Metal Organic Chemical Vapor Deposition, Jpn. J. Appl. Phys., Part 2, **44**, L1231 (2005).

[28] S. K. Singh and H. Ishiwara, Reduced Leakage Current in $BiFeO_3$ Thin Films on Si Substrates Formed by a Chemical Solution Method, Jpn. J. Appl. Phys., Part 2, **44**, L734 (2005).

[29] C. F. Chung, J. P. Lin, and J. M. Wu, Influence of Mn and Nb dopants on electric properties of chemical-solution-deposited $BiFeO_3$ films, Appl. Phys. Lett., **88**, 242909 (2006).

[30] C. C. Lee and J. M. Wu, Effect of film thickness on interface and electric properties of $BiFeO_3$ thin films, Applied Surface Science, **253**, 7069 (2007).

[31] C. Ternon, J. Thery, T. Baron, C. Ducros, F. Sanchette, J. Kreisel, Structural properties of films grown by magnetron sputtering of a $BiFeO_3$ target, Thin Solid Films, **515**, 481 (2006).

[32] J. K. Kim, S. S. Kim, and W. J. Kim, Sol-gel synthesis and properties of multiferroic $BiFeO_3$, Mater. Lett., **59**, 4006 (2005).

[33] S. Wha and C. Sung, Growth of multiferroics $BiFeO_3$ thin films by sol-gel method, J. Mag. Mag. Mat., **304**, 772 (2006).

[34] R. D. King-Smith, and D. Vanderbilt, Theory of polarization of crystalline solids, Phys. Rev. B, **47**, 1651 (1993).

[35] D. Vanderbilt and R. D. King-Smith, Electric polarization as a bulk quantity and its relation to surface charge, Phys. Rev. B, **48**, 4442 (1994).

[36] R. Resta, Macroscopic polarization in crystalline dielectrics: the geometric phase approach, Rev. Mod. Phys, **66**, 899 (1994).

[37] S. Fujino, M. Murakami, S. H. Lim, M. Wuttig, L.G. Salamanca-Riba, and I. Takeuchi, Ferroelectric properties of multiphase Bi-Fe-O thin films, Solid State Ionics, **178**, 1257 (2007).

[38] R. Bozorth, Ferromagnetism (Van Nostrand, New York, 1951), Rev. Mod. Phys, **19**, 29 (1947).

[39] A. Morrish, (1965), Physical Principles of Magnetism (New York: John Wiley and Sons).

[40] C. Kittel and J. K. Galt, Ferromagnetic Domains, Solid State Phys, **3**, 437 (1956).

[41] Kwan Chi Kao, (2004), Dielectric Phenomena in Solids, (California: Elsevier).

[42] C. Carter, and G. Norton, (2007), Ceramic Materials: Science and Engineering (New York: Springer).

[43] W. J. Merz, The electric and optical behavior of $BaTiO_3$ single domain crystals, Phys. Rev., **76**, 1221 (1949).

[44] W. Merz, Double Hysteresis Loop of $BaTiO_3$ at the Curie Point, Phys. Rev., **91**, 513 (1953).

[45] E. J. Huibregtse, and D. R. Young, Triple Hysteresis Loop and the Free-Energy function in the vicinity of the 5^0C Transition in $BaTiO_3$, Phys. Rev., **103**, 1705 (1956).

[46] P. Kharel, S. Talebi, B. Ramachandran, A. Dixit, V. Naik, M. Sahana, C. Sudakar, R. Naik, M. Rao, and G. Lawes, Structural, magnetic, and electrical studies on polycrystalline transition-metal-doped BiFeO3 thin films, J. Phys.: Condens. Matter., **21,** 036001 (2009).

[47] C.A. Kittel, (1996), Introduction to Solid State Physics, 7th ed. (New York: John Wiley and Sons).

[48] R. Melgarejo, M. Tomar, R. Guzman, and S. Singh, "Synthesis and Structural Characterization of $BiFeO_3$-$BaTiO_3$ Materials, Ferroelectrics, **324**, 101 (2005).

[49] A. Preumont, (2006), Mechatronics: Dynamics of Electromechanical and Piezoelectric Systems, 2nd ed., (Netherlands: Springer).

[50] S. W. Tsai, and H. T. Hahn, (1980), Introduction to Composite Materials (Lancaster: Technomic Publishing Company,).

[51] H. Schmid, Multi-ferroic magnetoelectrics, Ferroelectrics, **162**, 665 (1994).

[52] L. Martin, S. Crane, Y. Chu, M. Holcomb, M. Gajek, M. Huijben, C. Yang, N. Balke, and R. Ramesh, Multiferroics and magnetoelectrics: thin films and nanostructures, J. Phys.: Condens. Matter., **20**, 434220 (2008).

[53] W. Eerenstein, N. Mathur and J. Scott, Multiferroic and magnetoelectric, materials Nature, **442**, 759 (2006).

[54] N. A. Hill, Why are there so few magnetic ferroelectrics?, J. Phys. Chem. B, **104**, 6694 (2000).

[55] H. Schmid, Introduction to the proceedings of the 2nd international conference on magnetoelectric interaction phenomena in crystals, Ferroelectrics, **161**, 1 (1994).

[56] J. Rivera, On definition, units, measurements, tensor forms of the linear magnetoelectric effect and on a new dynamic method applied to Cr-Cl boracites, Ferroelectrics, **161**, 165 (1994).

[57] M. Lines, and A. Glass, (1977), Principles and Applications of Ferroelectrics and Related Materials, (Oxford: Clarendon Press).

[58] T. Lottermoser, T. Lonkai, U. Amann, D. Hohlwein, J. Ihringer, and M. Fiebig, Magnetic phase control by an electric field, Nature, **430**, 541 (2004).

[59] W. Brown, R. Hornreich, and S. Shtrikman, Upper bound on the magnetoelectric susceptibility, Phys. Rev., **168**, 574 (1968).

[60] A. Chen, and F. Chernow, Nature of ferroelectricity in KNO_3, Phys. Rev. **154**, 493 (1967).

[61] M. Saifi, and L. Cross, Dielectric properties of strontium titanate at low temperatures, Phys. Rev. B, **2**, 677 (1970).

[62] S. Hou, and N. Bloembergen, Paramagnetoelectric effects in $NiSO_4.6H_2O$, Phys. Rev. **138**, A1218 (1965).

[63] J. Scott, Mechanisms of dielectric anomalies in $BaMnF_4$, Phys. Rev. B, **16**, 2329 (1977).

[64] H. Grimmer, The piezomagnetoelectric effect, Acta Crystallogr. A, **48**, 266 (1992).

[65] Ryu, J., Vasquez-Carazo, A., Uchino K., and Kim, H.-E, Magnetoelectric properties in piezoelectric and magnetostrictive laminate composites, Jpn. J. Appl. Phys. **40**, 4948 (2001).

[66] H. Zheng, J. Wang, S. E. Lofland, Z. Ma, L. Mohaddes-Ardabili, T. Zhao, L. Salamanca-Riba, S. R. Shinde, S. B. Ogale, F. Bai, D. Viehland, Y. Jia, D. G. Schlom, M. Wuttig, A. Roytburd, and R. Ramesh, Multiferroic $BaTiO_3$-$CoFe_2O_4$ nanostructures, Science, **303**, 661 (2004).

[67] V. A. Murashov, D. N. Rakov, V. M. Ionov, I. S. Dubenko, Y. V. Titov, V. S. Gorelik, Magnetoelectric (Bi, Ln)FeO_3 compounds: Crystal growth, structure and properties, Ferroelectrics, **162**, 11 (1994).

[68] C. B. Sawyer, and C. H. Tower, Rochelle salt as a dielectric, Phys. Rev., **35**, 269 (1930).

[69] A. Souchkov, J. Simpson, M. Quijada, H. Ishibashi, N. Hur, J. Ahn, S. Cheong, A. Millis, and H Drew, Exchange Interaction Effects on the Optical Properties of $LuMnO_3$, Phys. Rev. Lett., **91**, 27203 (2003).

[70] Z. Cheng, X. Wang, S. X. Dou, H. Kimura, and K. Ozawa, Improved ferroelectric properties in multiferroic $BiFeO_3$ thin films through La and Nb codoping, Phys. Rev. B, **77,** 092101 (2008).

[71] M. Singh, H. Jang, S. Ryu, M. Jo, Polarized Raman scattering of multiferroic $BiFeO_3$ epitaxial films with rhombohedral $R3c$ symmetry, Appl. Phys. Lett., **88**, 42907 (2006).

[72] H. Fukumura, H. Harima, K. Kisoda, M. Tamada, Y. Noguchi, and M. Miyayama, Raman scattering study of multiferroic $BiFeO_3$ single crystal, J. Mag. Mag. Mat., **310**, e367 (2007).

[73] D. Kothari, V. R. Reddy, V. G. Sathe, A. Gupta, A. Banerjee, and A. M. Awasthi, Raman scattering study of polycrystalline magnetoelectric $BiFeO_3$, J. Mag. Mag. Mat., **320**, 548 (2008).

[74] Y. Wang, Q. Jiang , H. He and C. Nan, Multiferroic $BiFeO_3$ thin films prepared via a simple sol-gel method, Appl. Phys. Lett., **88,** 142503 (2006).

[75] N. X. Huang, L. F, Zhao, J. Y. Xu, J. L. Chen, and Y. Zhao, Effects of Substitution of Sm for Bi in $BiFeO_3$ Thin Films Prepared by the Sol-Gel Method, Chin. Phys. Lett, **27**, 027704 (2010).

[76] E. C. Subbarao, Ferroelectricity in $Bi_4Ti_3O_{12}$ and its solid solutions, Phys. Rev., **122**, 804 (1961).

[77] B. Aurivillius, Mixed bismuth oxides with layer lattices. I. Structure type of $CaCb_2Bi_2O_9$, Arkiv. Kemi., **1**, 463 (1949); B. Aurivillius, Mixed bismuth oxides with layer lattices: II. Structure of $Bi_4Ti_3O_{12}$, Arkiv. Kemi., **1**, 499 (1949).

[78] S. E. Cummings, and L.E. Cross, Electrical and optical properties of ferroelectric $Bi_4Ti_3O_{12}$ single crystal, J. Appl. Phys., **39**, 2268, (1968).

[79] P. C. Joshi, and S. B. Krupanidhi, Rapid thermally processed ferroelectric $Bi_4Ti_3O_{12}$ thin films, J. Appl. Phys. **72**, 5517 (1992).

[80] B. H. Park, S. J. Hyun, S. D. Bu, T. W. Noh, J. Lee, H.-D. Kim, T. H. Kim, and W. Jo. Differences in nature of defects between $SrBi_2Ta_2O_9$ and $Bi_4Ti_3O_{12}$, Appl. Phys. Lett, **74**, 1907 (1999).

[81] R. Melgarejo, M. Tomar, A. Hidalgo, and R. Katiyar, Sol-Gel derived $Bi_{4-x}Nd_xTi_3O_{12}$ Thin Films and Their Characterization, Mat. Res. Soc. Symp. Proc, **737** (2003).

[82] M. Maeder, D. Damjanovic, and N. Setter, Lead Free Piezoelectric Materials, J. Electroceram, **13**, 385, (2004).

[83] M. DeGuire, R. Ohandley and K. Gretchen, The cooling rate dependence of cation distributions in $CoFe_2O_4$, J. Appl. Phys, **65**, 3167 (1989).

[84] L. Hongri and S. Yuxia, Substantially enhanced ferroelectricity in Ti doped $BiFeO_3$ films, J. Phys. D: Appl. Phys. **40,** 7530 (2007).

[84] Lake Shore's fully integrated vibrating sample magnetometers (VSM), http://www.lakeshore.com/sys/vsm/vsmm.html.

[85] M. Tomar, D. Barrionuevo, S. Singh, R. Katiyar, Ferroelectric and ferromagnetic properties of Co doped $BiFeO_3$ thin films, **1256**, (2010)**.**

[86] D. Barrionuevo, S. Singh, M. Tomar, Structural, Magnetic, and Electrical Properties of $BiFe_{1-x}Mn_xO_3$ Thin Films, Mater. Res. Soc. Symp. Proc, **1199**, (2010).